Advances on Transition Metal Oxides Catalysts for Formaldehyde Oxidation: A Review

Abubakar Yusuf [a, b], Colin Snape [c], Jun He [a, b *], Honghui Xu [d], Chaojie Liu [a, e], Ming Zhao [f *], George Zheng Chen [a, c, e], Bencan Tang [a], Chengjun Wang [g], Jiawei Wang [h], Sailesh N. Behera [i]

[a] *Research Group of Natural Resources and Environment, Department of Chemical and Environmental Engineering, The University of Nottingham Ningbo China, Ningbo, PR China*
[b] *International Doctoral Innovation Centre, The University of Nottingham Ningbo China, Ningbo, PR China*
[c] *Faculty of Engineering, University of Nottingham, University Park, Nottingham, NG7 2RD, UK*
[d] *Zhejiang Meteorological Science Institute, Hangzhou, PR China*
[e] *Centre for Sustainable Energy Technologies, Faculty of Science and Engineering, The University of Nottingham Ningbo China*
[f] *School of Environment, Tsinghua University, Beijing 100084, China*
[g] *College of Chemistry and Materials Engineering, Wenzhou University, Wenzhou, PR China*
[h] *Aston Institute of Materials Research, Aston University, Birmingham, B4 7ET, UK*
[i] *Department of Civil Engineering, Shiv Nadar University, Greater Noida, U.P., India*

Correspondence:

Dr Jun He, email: jun.he@nottingham.edu.cn;

Dr Ming Zhao, email: ming.zhao@tsinghua.edu.cn

Abstract

This review highlights recent advances in the development of transition metal based catalysts for formaldehyde oxidation, particularly the enhancement of their catalytic activity for low temperature oxidation. Various factors that enhance low temperature activity are reviewed, such as morphology and tunnel structures, synthesis methods, specific surface area, amount and type of active surface oxygen species, oxidation state and density of active sites are discussed. In addition, catalyst immobilization for practical air purification, reaction mechanism of formaldehyde oxidation and the reaction parameters affecting the overall efficiency of the reaction are also reviewed.

Keywords: formaldehyde, transition metal oxides, catalysts, oxidation

1. Introduction

Formaldehyde (HCHO) is one of the main sources of hazardous indoor air pollution. Furniture and building materials such as composite wood, particle board, vinyl coverings and adhesives are some of the major indoor sources of HCHO emissions ([1,2]). A comprehensive review of both the indoor and outdoor sources of HCHO and its concentrations in various indoor environments can be found in the work of Salthammer et al. ([3]). Exposure to HCHO may cause adverse health effects on humans such as irritation to eyes, nose and throat, headache, fatigue, edema, severe allergic reaction and dermatitis ([4,5]). In 2006, the International Agency for Research on Cancer (IARC) under the World Health Organization (WHO) classified HCHO as a carcinogen to humans. There are sufficient evidences to ascertain that it causes nasopharyngeal cancer and there are also strong indications that it may also cause sinonasal cancer and leukemia over long term exposure ([6]). As such there are various international guidelines and recommended thresholds for indoor air HCHO concentrations, a summary of which can be found in the review of Salthammer et al. ([3]). The WHO proposes a short term HCHO exposure limit (30 minutes) of 0.1 mg/m^3 for the avoidance of sensory irritation and a long term exposure limit of 0.2 mg/m^3 for protection against long term health effects ([7]). Thus, the effective removal of HCHO from indoor air is imperative to improving indoor air quality and safeguarding human health.

Various techniques for HCHO removal have been investigated and reported in the literature, including adsorption ([8-12]), photo-catalytic oxidation ([13-17]) and catalytic oxidation (thermal and non-thermal). The effectiveness of physical adsorption of HCHO on adsorbents such as activated carbon (AC) is constrained by the material's maximum adsorption capacity, relative humidity (RH) or moisture deactivation and also by the environmental risk when desorption occurs during regeneration ([18,19]). Photo-catalytic oxidation using ultraviolent light on the other hand may lead

3

34   to the generation of toxic by-products (*20*). Catalytic oxidation is able to achieve complete

35   conversion of HCHO to H_2O and CO_2 without the formation of harmful by-products or secondary

36   pollutants (*21*). This could even be achieved at room temperature especially with noble metal

37   catalysts (*22-26*), thus making it the most promising HCHO removal technique (*18*).

38   Noble metal-based catalysts: Pt, Au, Pd, Rh, Ru and Ag supported on conventional materials such

39   as TiO_2, SiO_2, Al_2O_3 and zeolites (*27-35*); single transition metals (*36-47*) and transition metal-

40   based composites (*48-51*) exhibit excellent HCHO oxidation activities at temperatures lower than

41   100°C and even at room temperature. Comprehensive reviews on noble metal catalysts for HCHO

42   oxidation have been conducted (*4, 25*), whilst here a summary of some of the noble metal catalysts

43   and their reaction conditions are presented in Table 1. However, the industrial applications of noble

44   metal catalysts are restricted by their high costs, limited resources and poor thermal stabilities (*53*).

45   Hence recent research efforts have been focused on the development of relatively cheap materials

46   for low temperature HCHO catalytic oxidation (*54-56*). More abundant and cost effective metal

47   oxides especially those of the transition metals, including single transition metals and transition

48   metal based composites are shown to be active for HCHO oxidation. However their relatively low

49   activity compared to noble metals catalysts has motivated effort for further improvement.

50   Therefore, the development of highly active and cost effective catalysts for HCHO oxidation is

51   still a major challenge for practical application.

52   A number of review papers have been published on HCHO removal. Pei and Zhang (*52*) reviewed

53   chemisorption method and catalytic oxidation of HCHO majorly on noble metal catalysts. The

54   photo-catalytic oxidation of HCHO using TiO_2 as a photo-catalyst both in aqueous and gaseous

55   mediums and the effects of different light sources and photoreactors have also been reviewed in a

56   short article (*57*). More recently, Bai et al. (*4*) reviewed the catalysts for HCHO oxidation with a

57   major focus on the factors affecting the activity of noble metal catalysts. From the literature review,

58   it can be seen that significant progress has been made on improving the activity of transition metal

59   based catalysts and their immobilization for practical application since 2000. However, to the best

60   of our knowledge, the development of transition metal based catalysts for HCHO degradation has

61   not been reviewed in any detail so far. Therefore, we consider this review fills a key gap for this

62   active area of heterogeneous catalysis.

63   This review focuses exclusively and extensively on recent developments over the past one and half

64   decade towards enhancing the activity of transition metal catalysts for low temperature HCHO

65   oxidation, considering their cost reduction potential, activity and stability. Various factors that

66   enhance their catalytic activities are discussed, including preparation methods, morphology and

67   structure, specific surface area, concentration of surface active oxygen species, oxygen mobility

68   and metal active sites. The influence of reaction parameters such as relative humidity, HCHO

69   concentration and space velocity are also reviewed. The reaction mechanisms of HCHO oxidation

70   on transition metal oxides and their immobilization on suitable substrate materials for application

71   in air purification are also elaborated and finally areas for further investigations to achieve higher

72   activities at low temperatures are proposed.

73   **2. Transition metal based catalysts and their performances**

74   As mentioned earlier, recent research efforts have been focused on the utilization and efficiency

75   improvement of transition metal based catalysts for low temperature oxidation of HCHO.

76   Transition metal oxides are relatively cheap, abundant and have also been presented to be active

77   for HCHO oxidation at low temperatures (*21,67,68*). Different terminologies such as HCHO

78   removal, conversion, degradation and elimination are used in the literature to refer to the efficiency

79   of HCHO oxidation. Hereinafter, efficiency of HCHO oxidation is referred to as conversion where

80 oxidation efficiency was reported as a function of CO_2 generation/concentration in the effluent

81 stream and as removal where efficiency was reported based on residual HCHO concentration in

82 the effluent gas stream (see footnotes of Table 1&2).

83 Some conventional transition metal-based catalysts have been reported to show good catalytic

84 activities for HCHO oxidation. Sekine (*2*) first demonstrated the catalytic oxidation of HCHO over

85 metal oxide catalysts. Of the investigated catalysts: CoO, MnO_2, TiO_2, CeO_2 and Mn_3O_4, MnO_2

86 was described to exhibit the highest catalytic activity. Metal oxides in the conventional bulk form

87 possess low catalytic activity for HCHO oxidation owing to inferior surface properties (*69*). On

88 the contrary, specially synthesized nanostructured transition metal catalysts of similar

89 compositions to their bulk counterparts exhibit improved morphologies and surface properties and

90 hence higher activities for HCHO oxidation (*21,70*). As such, current investigations on transition

91 metal-based catalysts are focused on improving and developing materials with enhanced

92 morphologies and structures. The structure of these catalysts and their morphologies improve their

93 activity through the improvement of parameters (discussed in Section 4) such as specific surface

94 area, high surface reducibility, porosity, active surface species, active lattice and   surface

95 adsorbed oxygen species and tunnel size and structure (*54,55*). Transition metal-based catalysts

96 for HCHO oxidation found in the literature could basically be classified as single/mono-metal and

97 composite metal oxides. A summary of both group of catalysts and their activities and conditions

98 of reaction are respectively presented in Table 2 and 3.

99 2.1 Single transition metal based catalysts

100 *2.1.1 Manganese oxide based catalysts*

101 Manganese oxide is the most widely explored transition metal catalyst for HCHO oxidation owing

102 to its high catalytic activity, thermal stability, existence in various crystal morphologies such as α-

103   , β-, γ- and δ-MnO$_x$ (*71*) and several tunnel assemblies (1D tunnels, layered structures such as

104   birnessite and buserite and 3D spinel tunnel structures) (*72*).   Chen et al. (*55*) studied the

105   influence of tunnel structures of various manganese oxide catalysts (pyrolusite, cryptomelane and

106   todorokite) on HCHO oxidation. Cryptomelane displayed the highest activity with 100% HCHO

107   conversion at 140°C, 400 ppm HCHO concentration, and a space velocity of 18,000 mL/g·h, while

108   20 and 40% conversions were attained by pyrolusite and todorokite, respectively, under similar

109   reaction conditions. Tunnel size and structure were shown to be the determinant factors affecting

110   activity other than factors such as specific surface area, degree of crystallinity, surface reducibility

111   and average oxidation states of the catalysts. Similarly, Zhang et al. (*19*) attributed the high HCHO

112   catalytic activity of δ-MnO$_2$ to its interlayer and tunnel structures which help in expediting

113   adsorption and diffusion to and from the catalyst's active sites. These results indicate that activity

114   is closely related to morphological and structural properties of the catalyst.

115   Tian et al. (*54*) investigated the impact of synthesis temperature on birnessite type manganese

116   oxide catalysts. A general trend of catalytic activity rise was observed with increasing synthesis

117   temperature from 80 to 120°C. The catalyst synthesized at 120°C exhibited the highest activity

118   with a HCHO conversion of 100% at 100°C. This observed high activity was attributed to higher

119   surface reducibility, specific surface area, crystallinity and porosity compared to other catalysts

120   synthesized at different temperatures. Wang et al. (*73*) studied the effect of H$_2$O molecules on the

121   activity of birnessite manganese for HCHO oxidation at room temperature and indicated that

122   activity depends on the amount of both adsorbed H$_2$O molecules and interlayer hydroxyl and H$_2$O

123   molecules present in the catalyst. Interestingly, as the drying temperature increases from 30 to

124   500°C, so does the specific surface area, but activity dramatically decrease as displayed in Figure

125   1(a) due to the reduction in water content. This result indicates that the activity of birnessite is

126   more a function of the interlayer H_2O molecule content than specific surface area. The presence of

127   H_2O molecules enhances adsorption of HCHO molecules on the surface, conversion and

128   desorption of intermediates from the catalyst's surface.

129   Furthermore, the effect of manganese vacancy (V_{Mn}) on the activity of birnessite-type MnO_2 was

130   studied (74). Their results indicate that the presence of V_{Mn} improves the content of the surface

131   adsorbed oxygen containing species facilitated by the presence of interlayer K^+, which helps in

132   charge imbalance compensation caused by the created vacancy. The effect of surface pores created

133   by the modification of birnessite-MnO_2 with nitric acid and tetra-ammonium hydroxide on HCHO

134   oxidation was also investigated (75). The created defects as proposed by the authors served as sites

135   for activation of molecular oxygen and H_2O, hence resulting in the increased density of active

136   surface oxygen species and activity of the modified catalyst.

137   Tian et al. (56) also examined the effect of synthesis reaction temperature on the catalytic activities

138   of various cryptomelane manganese octahedral molecular sieve K-OMS-2 catalysts. The K-OMS-

139   2 nanoparticle catalyst prepared at room temperature exhibited a higher catalytic activity compared

140   to K-OMS-2 nanorod structured catalyst prepared at 100°C. The former attained 64% HCHO

141   conversion at the reaction temperature of 100ºC was due to the existence of a higher proportion of

142   pore channels compared to the 10% accomplished by the latter under the same reaction conditions.

143   Tian et al. (36) studied the relationship between textural properties and catalytic activity of the

144   cryptomelane manganese oxide catalyst, and showed that a resultant increase in textural properties

145   (specific surface area and pore volume) as a result of synthesis temperature increment from 15 to

146   70°C led to a dramatic improvement in catalytic activity.

147   Three dimensional mesoporous MnO_2 (3D MnO_2) catalysts prepared via nanocasting route using

148   KIT-6 hard template, which retain the mesoporous properties of the template were shown to be

149   promising for HCHO oxidation (*76*). The mesoporous structure, high specific surface area and

150   large number of surface active Mn^{4+} ions enhanced its high activity compared to the corresponding

151   α-MnO_2 and β-MnO_2 nanorod catalysts. Complete HCHO oxidation to H_2O and CO_2 was

152   accomplished at 130°C with 3D MnO_2 while same conversion was achieved at 140°C and 180°C

153   respectively with α-MnO_2 and β-MnO_2 under similar reaction conditions. This indicates that

154   activity is closely related to morphological structures of the catalyst. The catalytic activities of α,

155   β, γ and δ phase structures of MnO_2 were also investigated (*19*). The following order of activity

156   for complete HCHO oxidation was established: δ- > α- > γ- > β- MnO_2. Complete HCHO oxidation

157   was attained at 80°C on δ-MnO_2. Its high activity was suggested to be a function of its abundant

158   concentration of lattice oxygen species (see section 4.3 for further discussion on the roles active

159   surface oxygen species) and 2D layered structure, the latter of which enables easy adsorption and

160   diffusion of HCHO.

161   Chen et al. (*21*) prepared mesoporous hollow and honeycomb structured K_xMnO_2 nanospheres.

162   The former displayed higher activity of up to 100% HCHO removal at 80°C, while the latter

163   attained similar removal efficiency at 100°C under similar reaction conditions. Catalytic activity

164   of hollow structured K_xMnO_2 nanospheres was attributed to its porosity and the ability to retain

165   HCHO in its pores for a longer period compared to honeycomb structured catalyst. Zhou et al. (*77*)

166   examined the catalytic activity of various structures of Mn and the following order of decreasing

167   activity was established at reaction temperature below 120°C: cryptomelane Mn_2O > birnessite

168   Mn_2O > ramsdellite Mn_2O > monoclinic MnOOH. However, birnessite turns out to exhibit better

169   activity for complete HCHO oxidation at higher temperature, achieving 100% removal at 140°C

170   while cryptomelane at 160°C under similar conditions. This was possibly a result of weakened

171   HCHO adsorption on cryptomelane at lower temperature as suggested by the authors.

172   *2.1.2 Cobalt oxide based catalysts*

173   Cobalt oxide is another important transition metal-based oxide that has recently been attracting

174   attention for low temperature VOC catalytic applications. Similar to MnO_x, Co_3O_4 also exhibit

175   various morphologies which include nano-fibers (*78*), nano-sheets, nano-cubes, nano-rods (*79*)

176   and the morphologies influence its catalytic activity through the exposure of catalytically active

177   surface sites (*70*). The activity of Nano-, 2D- and 3D-Co_3O_4 structures for complete HCHO

178   oxidation was compared and the following order of reactivity was established: 3D-Co_3O_4 > 2D-

179   Co_3O_4 > nano-Co_3O_4 (*70*). The superior activities of 3D and 2D-Co_3O_4 was ascribed to their

180   mesoporous channel structure which enables easy diffusion of reactants to undergo reaction on the

181   active surface compared to the non-porous nano-Co_3O_4; in addition, the best performance of 3D-

182   Co_3O_4 was closely related to its abundant surface adsorbed oxygen species, large specific surface

183   area and exposed active Co^{3+} species on the (2 2 0) crystal face. Similarly, Ma et al. (*51*) indicated

184   that 2D-Co_3O_4 composed mainly of active Co^{3+} species on the (1 1 0) facet was able to achieve

185   20.3% HCHO oxidation at room temperature.

186   Fan et al. (*67*) investigated the effect of precipitants on the activity of Co_3O_4 catalysts. The catalysts

187   synthesized using carbonates and bicarbonates displayed better textural properties and superior

188   catalytic activities. The catalyst produced from $KHCO_3$ reached 100% HCHO conversion at 90°C,

189   compared to 120°C and 130°C for those prepared from KOH and $NH_3 \cdot H_2O$, respectively.

190   Recently, Wu et al. (*78*) described the utilization of porous Co_3O_4 nanofibers prepared by spiral

191   electrospinning and controlled calcination (500°C) as highly active catalysts for HCHO oxidation.

192   Complete oxidation was accomplished at 98°C under a space velocity of 30,000 mL/g·h and it was

193   shown to be highly stable for up to 160 hrs. Its activity was attributed to its high specific surface

194   area and large pore volume which provided more active sites for the reaction.

195   Despite the reported influence of morphological structure on the activity of Co_3O_4 based catalysts,

196   very few structures have been exploited for HCHO oxidation. There is therefore the need for

197   further work to investigate other structures such as nano-sheets, nano-cubes, nano-rods and the

198   extent to which they can influence other properties such as specific surface area, porosity and

199   exposure of active metal sites and active oxygen species for improved low temperature HCHO

200   oxidation.

201   *2.1.3 Other metal oxides*

202   Beside manganese and cobalt based catalysts, other metal oxides have been investigated in the

203   literature. Xia et al. (*69*) synthesized 3D ordered rhombohedra Cr_2O_3 using assisted ultrasound

204   nanocasting in the presence of 3D mesoporous silica (KIT-6) as template. The catalyst attained up

205   to 90% HCHO conversion at 117°C. The ultrasound assisted synthesis played a major role in

206   improving the characteristics and activity of the catalyst compared to similar catalysts synthesized

207   in the absence of ultrasound. Huang et al. (*80*) first recounted the use of bifunctional Eu-doped

208   CeO_2 with both thermal- and photo-catalytic oxidation capabilities for HCHO oxidation. Doping

209   Eu onto CeO_2 dramatically enhanced its HCHO oxidation activity and complete oxidation

210   temperature was reduced from 310°C on pure CeO_2 to 120°C on 4% Eu doped CeO_2. Catalytic

211   activity was promoted through oxygen vacancy creation on the surface of CeO_2, greater redox

212   ability, more abundant surface active Ce^{3+} and enhanced surface reaction. The created defects

213   provide more sites for oxygen activation hence providing more active surface oxygen species for

214   reaction. In addition, the catalysts exhibited an outstanding stability of up to 100 hrs on stream

215   without any sign of deactivation. Similarly, Zeng et al. (*81*) demonstrated that hydrogenation

216 treatment of TiO_2 and C-TiO_2 improved their activity through the creation of more surface oxygen

217 vacancy and surface hydroxyl groups. The untreated catalysts virtually displayed no activity for

218 HCHO oxidation in a static chamber reaction after 4 hrs at room temperature in the absence of

219 light illumination, while the treated catalysts including H-TiO_2 and H-C-TiO_2 were able to

220 respectively attain 53% and 57% removal under similar reaction conditions.

221 In general, manganese and cobalt based catalysts were demonstrated to be active compared to other

222 transition metals catalysts for HCHO oxidation. However, not much work has been done on other

223 transition metals. In order to explore their full potentiality as viable catalysts, further work is

224 needed to explore their utilization for low temperature HCHO oxidation. In addition, more work

225 is required to explore surface oxygen vacancy or defects creation using various dopants to improve

226 oxygen activation ability of metal oxide catalysts, to enrich active surface oxygen concentration

227 for enhanced low temperature reaction.

228 2.2 Transition metal-based composites/mixed oxides

229 Transition metal-based composites have been widely applied in the control of pollutants such as

230 CO (*83,84*) and ammonia (*85*). Composite catalysts for HCHO oxidation have also been

231 investigated and reported in the literature. These catalysts are generated by co-synthesis of two

232 transition metals oxides or the addition of other metal oxides either by co-precipitation (*48,86*) or

233 by other synthesis methods such as nanocasting (*51*). Composite catalysts were shown to exhibit

234 superior catalytic activities compared to the corresponding single materials synthesized using

235 similar procedure. This is due to synergistic or promotional influence of improved oxidation

236 capabilities either through higher surface oxygen mobility, creation of more oxygen vacancies

237 (*48,86*) or enhancing charge transport during redox cycles (*87*). To improve oxygen vacancy

238 formation in a composite catalysts and reduce the energy requirement for such, it was suggested

239 that the dopant should possess weaker M-O bonds; have larger radius and possess lower

240 electronegativity (*88*). Various composites such as MnO_x-CeO_2 (*48,86*), Co_3O_4-CeO_2 (*51*), MnO_2-

241 Fe_2O_3 (*89*), CuO-MnO_2 (*51,89*), MnO_x-SnO_2 (*90*), Co_3O_4-ZrO_2 (*91*) and Co-Mn oxide (*68*) have

242 been studied for HCHO oxidation.

243 *2.2.1 MnO_x-CeO_2 composites*

244 The composites of Mn and Ce oxides were shown to be active for HCHO oxidation owing to the

245 synergistic effect of Mn high activity and O_2 storage capacity of ceria. In addition, the composites

246 aid in attaining higher oxidation states for Mn (*83,92*) which is vital for HCHO oxidation (*87*).

247 Formation of solid solution between Mn and Ce is also critical to achieving synergistic influence

248 through O_2 transfer mechanism (*48,86*). Solid solution was shown to be attained in the Mn-Ce

249 molar ratio (Mn/(Mn + Ce)) range of 0.3 to 0.5, with 0.5 molar ratio being the optimum

250 composition (*48,86,93*) and the solubility limit for the substitution of Ce ions by Mn ions in the

251 composite (*53*).

252 Tang et al. (*86*) indicated that the manifestation of synergy in MnO_x-CeO_2 solid solution

253 composite, which enables the composite to attain complete HCHO conversion at lower

254 temperature (100°C) compared to pure MnO_x and CeO_2. The synergy was attained through a series

255 of redox cycles (Mn^{4+}/Mn^{3+} and Ce^{4+}/Ce^{3+}) involving the activation of molecular oxygen by Ce

256 and its transfer to Mn. The optimum calcination temperature for solid solution stability was shown

257 to be 550°C, above which activity decreased owing to phase segregation. In another investigation,

258 Tang et al. (*48*) further highlighted that above Mn-Ce molar ratio of 0.5, MnO_x crystallizes out of

259 the solid solution, with a consequent drastic reduction in catalytic activity, which is in conformity

260 with the findings of Li et al. (*93*). However, higher total decomposition temperature of 270°C was

261 reported by Li et al. (*93*) for $Mn_{0.5}Ce_{0.5}O_2$. Nonetheless, the catalysts were able to totally oxidize

262 HCHO at room temperature in the presence of 506 ppm ozone (O_3) in the feed stream. The ozone

263 molecules enhance the reaction by dissociating on the catalyst's surface and providing enough

264 atomic oxygen species to drive the reaction (*93*).

265 Quiroz et al. (*53*) studied the impact of acid treatment over MnO_x-CeO_2 composite for HCHO

266 oxidation. Their results indicated that the treatment had no pronounced effect on the textural and

267 redox properties of the composites within the solubility limit of Mn (Mn molar ratio ≤ 0.5) in

268 CeO_2. However, at higher Mn molar ratio (0.7 and 1) when MnO_2 began to crystallize out of the

269 solid solution, significant improvement in catalytic activity was observed owing to the increased

270 specific surface area and higher oxidation state of surface Mn. It is important to mention that while

271 textural properties of the solid solution were not altered by the acid treatment, the oxygen transfer

272 ability of CeO_2 was significantly hampered by the formation of $Ce(SO_4)_2$ resulting into a drastic

273 reduction in activity. Therefore, acid treatment has positive effects on pure MnO_2 and an inhibitive

274 effect on the synergy of the solid solution composites. The modification of birnessite-structured

275 MnO_2 with ceria for HCHO oxidation was also reported in the literature (*94*). The incorporation

276 of cerium ions inhibited the growth of MnO_2 crystals leading to particle size reduction and increase

277 in specific surface area, as the amount of doped ceria increases. The doping led to the increase in

278 the amount of oxygen vacancies and the rate of molecular oxygen activation into surface adsorbed

279 oxygen species (O_2^-, O^- or terminal hydroxyl (OH) group (*74*)). The catalyst with the highest ratio

280 of surface adsorbed oxygen to lattice oxygen exhibited the best catalytic performance. At higher

281 ceria doping (Ce-MnO_2, molar ratio 5:10), the birnessite structure collapsed leading to decrease in

282 catalytic activity.

283 Tang et al. (*48*) further demonstrated that impregnating Pt on MnO_x-CeO_2 composite significantly

284 improved its activity by attaining 100% HCHO conversion at room temperature as shown in Table

285 1. It is noteworthy to mention that the formed composite (Pt/MnO_x-CeO_2) was prone to

286 deactivation with increasing HCHO concentration. Its activity dropped from 100% conversion at

287 30 ppm to 54% in the presence of 580 ppm HCHO at room temperature as shown in Figure 2.

288 Meanwhile the same authors (*86*) showed that MnO_x-CeO_2 composite was stable for complete

289 HCHO oxidation over 48 hrs without any sign of deactivation at similar concentration (580 ppm).

290 It should however be noted that the latter experiment was conducted at 100°C and the high

291 temperature could aid the decomposition of intermediate species while the former was conducted

292 at room temperature. This indicates that Pt might be prone to deactivation by HCHO at higher

293 concentration, which needs to be investigated further.

294 *2.2.2 Co_3O_4-CeO_2 composites*

295 Ma et al. (*51*) investigated the oxidation of HCHO at room temperature on 2D-Co_3O_4-CeO_2

296 composites. They discovered that no synergy or activity improvement was realized by the formed

297 2D-Co_3O_4-CeO_2 composites and that 2D-Co_3O_4 was more active than the composites with

298 respective HCHO conversions of 13.2% and 20.3% at room temperature. It should however be

299 noted that no solid solution formation was observed in the 2D-Co_3O_4-CeO_2 composites, which is

300 a phenomenon reportedly required for achieving synergy through ceria O_2 transfer mechanism

301 (*48,86*). The incorporation of Au in the composite (2D-Au/Co_3O_4-CeO_2) improved the composite's

302 activity to 50% conversion at room temperature (Table 1) by promoting desorption of surface

303 active oxygen species (*51*). Liu et al. (*50*) presented the evidence of solid solution formation in 3D

304 ordered macroporous (3DOM) CeO_2-Co_3O_4 catalysts with low loading of Co_3O_4. However, the

305 3D-CeO_2-Co_3O_4 catalysts with various Ce-Co molar ratios were shown to possess low catalytic

306 activities. Loading Au particles (3 wt. %) on the composites distinctively improved their catalytic

307 activities, and in fact all the Au supported composites were able to completely convert HCHO into

15

308 CO$_2$ and H$_2$O below 65°C. The composites (3D Au/CeO$_2$-Co$_3$O$_4$), with lower Co content in CeO$_2$-

309 Co$_3$O$_4$ in the region solid solution, presented better activity in this study. When higher Co molar

310 ratios was employed, segregation between CeO$_2$ and Co$_3$O$_4$ occurred, which led to weaker

311 interaction and thus reduced the activity of the Au/CeO$_2$-Co$_3$O$_4$ catalysts.

312 *2.2.3 Co-Mn oxides Composites*

313 The composites of Co and Mn oxides were also studied and shown to be more active than the

314 individual pure oxides for HCHO complete oxidation (*95*). Favorable synergy was obtained due

315 to the abundant surface adsorbed oxygen species generated by the oxygen vacancies created in the

316 Co-Mn oxides solid solution. Textural and redox properties were also shown to be affected by the

317 synthesis method employed. Co-precipitation synthesis produced a more active catalyst with

318 higher specific surface area, higher relative content of surface adsorbed oxygen species and surface

319 active manganese (Mn^{4+}) that completely oxidized HCHO at 75°C compared to 100°C over that

320 synthesized using sol-gel method.

321 Wang et al. (*68*) further studied the efficiency of the cycling "storage-oxidation" process for

322 HCHO oxidation using 3D ordered mesoporous Co-Mn oxides composite (3D-Co-Mn)

323 synthesized using KIT-6 template and that of Co-Mn oxides composite synthesized using co-

324 precipitation. During the storage process, the catalysts were first exposed to a feed stream of O$_2$

325 and HCHO; subsequently, the stored HCHO was oxidized in a flow of O$_2$ at elevated temperature

326 to evaluate its activity. The 3D-Co-Mn oxides composite was shown to have superior storage

327 capacity of up to 0.8 mmol/g-catalyst and HCHO complete oxidation temperature of 70°C,

328 compared to the storage capacity of 0.428 mmol/g-catalyst and HCHO complete oxidation

329 temperature of 75°C respectively achieved by co-precipitated Co-Mn oxides composite. The

330   excellent activity of 3D-Co-Mn oxides composite was attributed to its larger specific surface area

331   and ordered mesoporous structure. Lu et al. (*96*) studied HCHO oxidation over MnO_x-Co_3O_4-CeO_2

332   composites and found out that the incorporation of MnO_x into Co_3O_4-CeO_2 greatly improved its

333   textural properties and the amount of available surface active oxygen species, resulting in an

334   improvement in catalytic activity.

335   *2.2.3 Other Composites*

336   Other composites such as MnO_x-SnO_2 (*90*) and zirconia supported cobalt oxide catalysts (*91*) have

337   been reported in the literature. Wen et al. (*90*) showed that the redox properties of MnO_x-SnO_2,

338   which were in turn influenced by the preparation method, played a crucial role in determining its

339   activity. Their experimental results highlighted that higher oxidation states of Mn were more active

340   in HCHO oxidation. The dominant oxidation state of Mn in the composite synthesized using redox

341   co-precipitation was Mn^{4+} while Mn^{3+} was the main state in the co-precipitated composite, which

342   accounted for the difference in their activities as shown in Table 3. This is in agreement with other

343   reported literatures for the active state of Mn for HCHO oxidation (*76,86*). Lu et al. (*87*)

344   investigated the catalytic performance of graphene-MnO_2 (G-Mn) hybrid for complete oxidation

345   of HCHO. The G-Mn hybrid catalyst achieved complete HCHO conversion at 65°C, compared to

346   140°C for pure MnO_2 and the completely inactive graphene (G) nanosheets. The hybrid system

347   exposed more Mn^{4+} active sites, enhanced charge transport during Mn redox cycle and offered a

348   larger amount of surface HYDROXYL species which eased HCHO oxidation and improved

349   activity.

350   **3. Catalyst immobilization on porous materials for practical HCHO oxidation**

351   For practical applications, deployment of powdered form materials especially nanosized, gives rise

352   to engineering challenges such as dust contamination and nanoparticle leaching in flue gas streams

353 (*82*). Therefore, catalysts immobilization on porous materials with low air pressure drop is

354 considered viable for air purification processes. A variety of porous materials with low air

355 resistance including polyethylene terephthalate (PET) (*18*), polyester particulate filter (*97*) and

356 porous cellulose fiber (*82*) have been used as supporting materials for immobilizing nanoparticle

357 catalysts for HCHO oxidation. A summary of the activity of these immobilized catalysts is

358 presented in Table 4. Wang et al. (*18*) reported the in-situ coating of δ-MnOx nanosheet on the

359 surface of PET first through surface reaction followed by in-situ deposition. The formed composite

360 which is light with low air resistance and high specific surface area, proved highly active and stable

361 for low concentration HCHO (0.6 mg/m^3) oxidation at room temperature for 10 hrs. Sidheswaran

362 et al. (*97*) supported Mn based catalyst with 84% nsutite, 2% cryptomelane and 13% manjiroite

363 composition on the surface of a thin polyester particulate filter for heating ventilation and air

364 conditioning (HVAC) and evaluated its performance for HCHO oxidation. Experimental results

365 indicated that stable single pass HCHO oxidation with over 80% removal efficiency at room

366 temperature was achieved continuously for 35 days for both high and low face velocities close to

367 typical building air ventilation systems.

368 Zhou et al. (*82*) likewise demonstrated an in situ deposition of MnO_2 nanosheets on cellulose fiber

369 composite (8.86 wt.% MnO_2/cellulose fiber) and showed that even though birnessite powder is

370 slightly more active than the composite (100% and 99.1% at 140°C, respectively), the composite

371 is about 19 times more active in terms of HCHO removal per mg of MnO_2. However, the observed

372 difference could supposedly be attributed to the removal/adsorption capacity of cellulose fiber and

373 not necessarily HCHO conversion as CO_2 generation and catalytic activity of the cellulose fiber

374 were not monitored in the experiment. Li et al. (*98*) and Dai et al. (*71*) respectively utilized AC for

375 immobilizing birnessite-MnO_2. In both cases, HCHO was completely converted into CO_2 in a

376   static reaction chamber. However, the conversion patterns in the individual experiments were such

377   that the concentration of HCHO sharply dropped in the first 60 mins with little corresponding CO_2

378   generation, possibly indicating that the molecules were actually adsorbed onto the surface of AC.

379   The adsorbed molecules were consequently and slowly converted into CO_2 over 6 hrs (*98*) and 9

380   hrs on birnessite-MnO_2/AC (*71*) respectively as shown in Figure 3(a&b). Similar patterns were

381   observed over unsupported birnessite as shown in Figure 1(b) (*73*). In contrast, simultaneous

382   HCHO conversion and CO_2 generation were observed over modified birnessite with manganese

383   vacancies and up to 81.7% conversion was attained in the first one hour of the static experiment

384   (*74*). This indicates that the HCHO is instantaneously converted into CO_2, as opposed to the AC

385   supported birnessite (*71,98*) in which the HCHO is adsorbed onto the AC and subsequently

386   converted over time. Few immobilized transition metal-based catalysts for HCHO oxidation have

387   been reported as presented in Table 4; therefore, further investigations are required to evaluate

388   more effective substrate materials for immobilization and to understand their interactions with the

389   catalysts and effectiveness for practical application in air purification process. In addition, these

390   materials need to be tested under indoor conditions in air purifiers or HVAC systems and evaluate

391   the effect of conditions such as particle leaching, dust contamination, relative humidity and

392   temperature variation, on the effectiveness and stability of these materials.

393   **4. Influence of catalyst based factors on HCHO oxidation efficiency**

394   The effectiveness of HCHO oxidation process is majorly related to the activity/reactivity of the

395   catalyst deployed and other reaction parameters such as temperature, concentration, space velocity,

396   catalyst mass and relative humidity. Catalytic activity is in turn influenced by a number of

397   physicochemical properties which include structure and morphology, preparation or synthesis

398   method, degree of crystallinity, surface reducibility, specific surface area, amount of active oxygen

399 species and active metal sites (*54*). A combination of these properties is decisive for high catalytic

400 activity and for an effective HCHO oxidation at low reaction temperature.

401 4.1 Influence of synthesis methods and conditions on textural properties, morphology and

402 activity

403 Several conventional preparation methods can be used to synthesize catalysts for HCHO oxidation

404 including sol-gel method (*56*), precipitation and co-precipitation (*86,97*). Recent researches have

405 mainly focused on improving and modifying catalysts preparation methods to enhance their

406 performance and catalytic activities through the utilization of synthesis techniques such as

407 hydrothermal synthesis (*77*), electrospinning (*78*), electrodeposition (*80*) and hard template

408 nanocasting (*70,76*). Synthesis methods and reaction conditions are able to tailor catalysts' textural

409 and surface properties, structures and morphologies (as shown in Figure 4 (*77*)) and hence

410 influence their catalytic activity (*36,54*) as shown in. For instance, the utilization of ultrasound

411 assisted nanocasting of 3D-Cr_2O_3 using KIT-6 as template helps in enhancing the penetration of

412 precursor materials into the mesoporous structure of KIT-6, which proved efficient in improving

413 its specific surface area, pore volume and mesoporousity compared to 3D-Cr_2O_3 synthesized

414 without the aid of ultrasound (*69*). Zhang et al. (*19*) highlighted that by varying reaction conditions

415 in a hydrothermal synthesis, various crystal structures of MnO_2 including: α- and δ-MnO_2; β- and

416 γ-MnO_2, with entirely different properties can respectively be produced from the same starting

417 materials.

418 Reaction temperatures in hydrothermal synthesis have tremendous effects on morphology and

419 structural evolution of structured manganese catalysts. Tian et al. (*54*) highlighted that the reaction

420 temperature greatly affects the crystallinity, surface reducibility, specific surface area and activity

421 of birnessite structured manganese oxide catalysts. At low synthesis temperature of 80°C, poorly

20

422   crystalline birnessites were produced, whilst the birnessites were transformed into well-crystalline

423   structures when reaction temperature was increased to 100°C, thereby increasing its activity.

424   However, higher temperature (140°C) led to decomposition of the birnessite structure as a result

425   of excessive reduction of Mn^{7+} by benzyl alcohol during the synthesis. Zhou et al. (*77*) also

426   observed that birnessites structure obtained at 120°C synthesis temperature transformed into

427   monoclinic MnOOH at 150°C and eventually collapsed into 1D MnOOH nanorods at 180°C as

428   shown in Figure 4. Similarly, a correlation between synthesis temperature and catalyst's

429   morphology for cryptomelane-type manganese octahedral molecular sieve (K-OMS-2) was

430   reported by Tian et al. (*56*). The morphologies of the K-OMS-2 catalysts changed from

431   nanoparticles at room temperature to nanorods at reaction temperatures of 80-100°C and to

432   nanowires at 120°C.

433   Tian et al. (*36*) reported that essential properties of cyptomelane catalyst such as morphology,

434   crystallinity, specific surface area and pore structure could be tailored by manipulating the

435   hydrothermal synthesis temperature. Increasing synthesis temperature distinctively raised the

436   crystallinity and textural properties of the catalyst. However, too high temperatures diminished

437   crystallinity and this is in agreement with the findings of Tian et al. (*54*) for birnessite manganese

438   catalysts. Textural properties such as specific surface area and pore volume were also shown to

439   vary with the synthesis temperature. An increase in the synthesis temperature led to a dramatic

440   improvement in textural properties: specific surface area and pore volume increased from 68 m^2/g

441   and 0.2 cm^3/g at synthesis temperature of 15°C, to 206 m^2/g and 0.3 cm^3/g at 70°C, respectively.

442   Such an improvement in textural properties in turn led to enhancement in catalytic activity.

443   Calcination temperature was also demonstrated to be very critical for catalysts structural stability

444   and activity. Wang et al. (*73*) indicated that between 30 and 300°C only a little change was

445 observed in the sizes of birnessite nanospheres and that the structure was prevented from

446 collapsing by interlayer K^+ and H_2O molecules present. However, when the calcination

447 temperature reached up to 500°C, the layered structure of birnessite completely collapsed and

448 transformed into cryptomelane with a 2×2 tunnel structure due to the loss of interlayer H_2O

449 molecules. The calcination temperature of composite MnO_x-CeO_2 prepared using modified co-

450 precipitation was shown to greatly influence its catalytic activity for HCHO oxidation (*86*). As the

451 temperature rises from 300-500°C, the relative amount of surface active Mn^{4+} and lattice oxygen

452 also rises, however at higher temperature (700°C) both the activity and the relative amount of

453 lattice oxygen dramatically decreased due to phase segregation evident by the appearance of MnO_2

454 crystals in the otherwise solid solution composite. Likewise, Wu et al. (*78*) indicated that high

455 calcination temperatures (600-800°C) led to the decrease in the activity of Co_3O_4 nanofibers as a

456 result of aggregation growth and collapse of the catalyst's mesoporous structure.

457 The utilization of templates and surfactants in catalysts synthesis for HCHO oxidation is also

458 attracting attention. When templates are deployed in catalyst preparation, the catalyst's structures

459 and morphology could easily be manipulated to enhance their catalytic activities (*56,76*) and

460 replicate the characteristics of the template materials used. While Shi et al. (*95*) demonstrated that

461 Co-Mn oxides composites prepared using co-precipitation method were far more active than those

462 prepared using sol-gel method, the same group (*68*) further disclosed that 3D mesoporous Co-Mn

463 oxides synthesized using KIT-6 hard template possessed superior activity owing to their better

464 textural properties. Similarly, the synthesis of 3D-Cr_2O_3 (*69*), 3D-Co_3O_4 (*70*) and 3D-MnO_2 (*76*)

465 have been demonstrated using KIT-6 molecular sieve hard template for HCHO oxidation. The

466 presence of the template improved the mesoporous structure and specific surface area and exposes

467 more active sites thereby enhancing catalytic activity. Other mesoporous structures including 2D-

468   MnO$_2$ (99) and 2D-Co$_3$O$_4$ (51,70) have been prepared using SBA-15 hard templates, which turned

469   out to be more active than the corresponding non-porous materials but less active than their 3D-

470   counterparts. Furthermore, Tian et al. (56) highlighted that highly active nanoparticle

471   cryptomelane (K-OMS-2) catalyst could be synthesized at room temperature with the aid of

472   cetyltrimethylammonium bromide (CTAB) surfactants without necessarily the use of high reaction

473   temperature as earlier reported (36).

474   Acidity of the reaction medium and the type of acid deployed in controlling the pH have significant

475   effects on the morphology of manganese based catalysts. Chen et al. (21) showed that mesoporous

476   hollow and honeycomb K$_x$MnO$_2$ nanospheres with varying properties and activities could be

477   produced by varying the ratio of KMnO$_4$ and oleic acid during the synthesis process. Zhou et al.

478   (77) revealed that introducing H$_2$SO$_4$ (decreasing the pH) into a reaction medium that would

479   otherwise produce birnessite structured manganese led to the production of cryptomelane

480   structured manganese. However, the type of anions present in the acid is also critical in

481   determining the resultant morphology under similar conditions. While the addition of H$_2$SO$_4$ led

482   to cryptomelane structure, addition of H$_3$PO$_4$ and HNO$_3$ produced birnessite and ramsdelite

483   structured manganese, respectively as shown in Figure 4. This shows that different anions play

484   dissimilar roles in channeling the mechanism of crystal formation towards a particular

485   morphology.

486   4.2 Influence of catalyst's morphology on activity

487   Catalysts' morphology and structure play an important role in promoting catalytic activities.

488   Control over the morphological structure of catalysts is able to influence other properties such as

489   pore size, specific surface area and the exposure of available surface active sites. The activity of

490   manganese oxide catalysts with square tunnel structures (pyrolusite, cryptomelane and todorokite)

491 is majorly affected by their tunnel sizes (*55*). Similarly the available surface active sites depend on

492 the nature of the catalysts. 3D- MnO_2 catalyst have more exposed Mn^{4+} on its crystal lattice plane

493 thereby improving its activity compared to the one-dimensional α-MnO_2 and β-MnO_2 nanorod

494 materials (*76*).

495 Chen et al. (*55*) investigated the effect of MnO_x tunnel structure on the active oxidation of HCHO

496 as shown in Figure 5. Three types of Mn tunnel structures were investigated including pyrolusite

497 with tunnel structure of ca. 0.23×0.23 nm^2, cryptomelane consisting of double edge sharing MnO_6

498 octahedral with tunnel diameter of ca. 0.46×0.46 nm^2 and todorokite composed of triple chains

499 edge-sharing MnO_6 with tunnel of ca. 0.69×0.69 nm^2. Experimental results indicated that

500 cryptomelane had the highest catalytic activity achieving 100% HCHO conversion at 140°C.

501 Cryptomelane possesses an effective tunnel diameter close to HCHO's dynamic diameter (0.234

502 nm) thereby allowing better adsorption and higher catalytic activity (*55*). Yu et al. (*41*) indicated

503 that the micropore channel structure of nest- and urchin-like MnO_2 improved their catalytic activity

504 by allowing better adsorption of HCHO compared to that of cocoon-like MnO_2 without mesopores

505 present despite having higher specific surface area.

506 Tian et al. (*54*) also highlighted that the presence of smaller catalytic pore sizes could extend the

507 residence of HCHO molecules in the catalyst's pores thereby improve its oxidation efficiency.

508 Correspondingly, the work of Tian et al. (*56*) underscored that the pore structures of nanoparticle

509 K-OMS-2 were readily accessible to HCHO molecules, enhancing higher adsorption and better

510 activity compared to K-OMS-2 nanorods with similar specific surface areas. Zhang et al. (*19*)

511 further highlighted that the 2D layered tunnel structure of δ-MnO_2 enhanced its activity through

512 facilitating the adsorption and desorption of HCHO to active sites compared to other structures (α-

513 , β- and γ- MnO_2). In another research, Chen et al. (*21*) stressed that catalyst's activity depends

514   more on its porosity and nanoplatelets crystal size than specific surface area. Mesoporous hollow

515   K_xMnO_2 nanospheres, which have smaller nanoplatelets size and specific surface area twice less

516   than those of its corresponding mesoporous honeycomb structure, achieved higher activity in

517   HCHO oxidation.

518   Wang et al. (*73*) showed that the structure of birnessite is such that it contains HYDROXYL groups

519   and H_2O molecules at the interlayer surface. The presence of these molecules greatly improved its

520   catalytic activity for HCHO removal even at room temperature. After the removal of both the

521   hydroxyl groups and H_2O molecules at high temperature, the birnessite structure collapsed and the

522   catalyst lost its high activity. Likewise, Sidheswaran et al. (*97*) indicated that the existence of H_2O

523   molecules in interstitial voids of MnO_2 based catalysts with varying composition of nsutite,

524   cryptomelane and pyrolusite contributed to its higher catalytic activity compared to 99% pyrolusite

525   catalyst which has smaller tunnel structure and lower H_2O molecules content in its interstitial

526   voids.

527   4.3 Roles of active surface oxygen in HCHO oxidation

528   It is reported in the literature that surface oxygen species either in the form of surface adsorbed

529   oxygen species (O_2^-, O^- or terminal hydroxyl (OH) group (*74*)) and lattice oxygen are critical to

530   the effectiveness of the catalytic oxidation of HCHO and other intermediates into CO_2 and H_2O

531   (*51,67,95*). However, there is a discrepancy regarding the respective roles of each type of oxygen

532   specie for HCHO oxidation over transition metal based catalysts. For example, Zhang et al. (*19*)

533   stipulated that since HCHO oxidation was shown to conform to Mars van Krevelen mechanism,

534   abundant lattice oxygen on the catalyst surface will lead to higher catalytic activity. They further

535   showed that the catalytic activities of four MnO_2 catalysts (α, β, γ and δ-MnO_2) are closely linked

536   to their respective amount of surface lattice oxygen (relative to surface adsorbed oxygen species)

537 and the following order of activity was established: δ- > α- > β- > γ- MnO_2. Similarly, Tang et al.

538 (*86*) indicated that the catalytic activity trend of MnO_x-CeO_2 composite catalysts synthesized using

539 various methods, followed the trend of their relative lattice oxygen content. Those richer in lattice

540 oxygen relative to surface adsorbed oxygen presented better activity.

541 On the other hand, surface adsorbed oxygen species were shown to be directly involved in the

542 activation of HCHO and its subsequent oxidation into CO_2 and H_2O (*74,75*). It was shown that the

543 activity of layered birnesite-MnO_2 catalysts with surface pits corresponds to the relative amount

544 of surface adsorbed oxygen species on the catalysts (*75*). The surface pits acts as vacancies for

545 activation of molecular oxygen and or H_2O into surface adsorbed oxygen and the higher the

546 relative amount of these species the better the catalytic activity. Wang et al. (*94*) contended that

547 while surface adsorbed oxygen species participates in the oxidation reaction of HCHO, lattice

548 oxygen species enhance their formation through its complex interaction with oxygen vacancy and

549 molecular oxygen. Huang et al. (*80*) reported that the enhancement of the relative amount of

550 surface adsorbed active oxygen species was achieved through the creation of surface defects by

551 doping Eu on CeO_2. The created oxygen vacancies served as sites for oxygen activation into active

552 superoxide (O^{2-}) species which could partake in surface reaction, hence enhancing the

553 concentration of surface adsorbed oxygen and the catalyst's activity. Similarly, surface defects

554 created on birnesite-MnO_2 catalysts served as pits for activation of molecular oxygen and H_2O into

555 surface active oxygen species, hence increasing the surface density of these species leading to

556 higher catalytic activity (*74,75*). Ma et al. (*51*) also underscored the role of surface adsorbed

557 oxygen (O^{2-}, O^-) in HCHO oxidation over cobalt based catalysts. They showed that catalytic

558 activity is closely associated to the ease with which active surface oxygen desorb from catalysts

559 surface. They further demonstrated that catalytic activity can be improved by increasing the ease

560   with which surface active oxygen desorb from catalyst's surface through the incorporation of Au

561   nanoparticles into Co_3O_4-CeO_2 composite. Likewise, it was demonstrated that 3D-MnO_2 with

562   abundant concentration of surface adsorbed oxygen species which easily desorb from the catalyst

563   at lower temperature exhibited better catalytic activity compared to 2D- MnO_2 with lower surface

564   adsorbed oxygen species concentration and nano-Co_3O_4 with virtually no active oxygen species

565   (O^{2-}, O^-) present (*70*).

566   In addition, Lu et al. (*87*) indicated that surface adsorbed oxygen species (hydroxyl group) and not

567   lattice oxygen are responsible for the high activity of graphene-MnO_2 hybrid catalyst for HCHO

568   oxidation. They further pointed out that the abundant relative amount of surface adsorbed hydroxyl

569   group on the catalyst did not only improve its catalytic activity but also simplified HCHO

570   conversion pathway by direct hydroxyl ion oxidation of formate species to CO_2 without the

571   formation of CO intermediates. It was also shown that surface adsorbed hydroxyl groups were

572   directly involved in the room temperature oxidation of HCHO on the surface of birnessite, which

573   led to the formation of formates and carbonates (*73*). Similarly, Wang et al. (*18*) showed that the

574   high amount of surface adsorbed oxygen in the form of hydroxyl species were responsible for the

575   high HCHO oxidation activity of δ-MnO_2/PET at room temperature. Similarly, Fan et al. (*67*)

576   underscored that hydroxyl species on the surface of Co_3O_4 are the key active surface oxygen

577   required for the formation of dioxymethylene (DOM) species and their subsequent conversion to

578   formate species in HCHO oxidation process.

579   4.4 Influence of reducibility and active metal sites on catalysts surface

580   The surface reducibility of catalysts plays an important role in determining their catalytic activity.

581   It indicates the amount of reactive species on the catalyst's surface and their onset reaction

582   temperatures (*54*). It could also indicate catalyst's oxygen mobility, which might cause more

583 oxygen adsorption and further excitement to active oxygen species which participate in the

584 oxidation reaction (19). Tian et al. (54) indicated a correlation between reduction temperature and

585 catalytic activity for birnessite manganese based catalysts. The established trend disclosed that the

586 lower the catalyst's reduction temperature (higher surface reducibility), the higher its HCHO

587 oxidative activity and vice-versa. Tang et al. (86) presented that owing to solid solution formation,

588 MnO_x-CeO_2 catalysts possessed higher surface reducibility and better catalytic activity compared

589 to pure MnO_x and CeO_2. Furthermore, the catalysts' activity reduced as surface reducibility

590 decreased (high reduction temperature) with increasing calcination temperature because of phase

591 segregation. Xia et al. (69) also indicated that chromia catalysts with the highest reducibility

592 possessed the best HCHO catalytic activity. Similar trends was also reported for HCHO oxidation

593 over Co_3O_4 catalysts (67).

594 The active sites present on catalyst's surface are critical and key for determining activity. The

595 higher the concentration or availability of exposed active metal sites on catalyst's surface, the

596 better its HCHO oxidative activity. Bai et al. (70) presented that Co^{3+} ions are the surface active

597 state and sites of 3D-Co_3O_4 for HCHO oxidation. The (220) crystal plane of the catalyst is

598 majorly composed of Co^{3+} against the Co^{2+} present on the (111) crystal plane of nano-Co_3O_4,

599 thereby making it more active and achieving complete HCHO oxidation at lower temperature.

600 Similarly, Ma et al. (51) demonstrated that the (110) facet of 2D-Co_3O_4 which is mainly composed

601 of Co^{3+} is the key active facet for effective HCHO oxidation. High activity for HCHO oxidation

602 by 3D-$MnO2$ was attributed to the presence of high content of Mn^{4+} active sites on the exposed

603 (110) crystal plane surface (76). These exposed ions provided sufficient sites upon which the actual

604 oxidation reaction takes place, thereby improving its activity. It was also shown that Mn^{4+} is the

605 active state and site for HCHO oxidation for MnO_x-CeO_2 based composite and the catalyst with

606   the highest amount of Mn^{4+} possessed the best activity (*48,86,87*). Zhang et al. (*19*) also

607   highlighted that amongst their investigated catalysts (α, β, γ and δ-MnO_2), those with the highest

608   content of Mn^{4+} displayed the best HCHO catalytic activity. Improving the electrochemical

609   properties of catalysts was proven to enhance their catalytic activities. Lu et al. (*87*) established

610   that the charge transport ability and interfacial electron transfer of MnO_2 during Mn^{4+}/Mn^{3+} redox

611   cycle can be enhanced by incorporating graphene into MnO_2 (G-Mn hybrid), which was revealed

612   to improve the electrical conductivity of MnO_2 and decrease electron transfer resistance. In

613   addition, it offered high specific surface area and 2D plane structure for increased exposure of

614   metal surface active sites (*100*).

615   4.5 Influence of specific surface area on HCHO catalytic activity

616   Catalysts' specific surface area is an important parameter affecting HCHO catalytic oxidative.

617   High specific surface area could enhance adsorption of HCHO molecules onto the catalyst's

618   surface and help in exposing more surface active sites, improving surface lattice defect and oxygen

619   vacancy, thereby leading to abundant surface active oxygen species (*70,78*), which is a key

620   requirement for oxidation reactions. A correlation between catalyst's surface and activity was

621   established by Wu et al. (*78*) for Co_3O_4 nanofibers. Activity increase was observed with increasing

622   specific surface area and pore volume as the calcination temperature increased from room

623   temperature to 500°C, above which a decline in activity was observed due to the destruction of the

624   mesopores and the consequent decrease in specific surface area at higher temperatures. Tian et al.

625   (*36*) also demonstrated that higher specific surface area greatly enhanced catalytic activity for

626   HCHO oxidation. Nanoparticle cryptomelane catalyst, with specific surface area as high as 206

627   m^2/g and smaller uniform mesopores exhibited higher catalytic activity than the corresponding

628   nanorod cryptomelane catalyst with a specific surface area of 68 m^2/g. The high specific surface

29

629 area and small nanoparticle sizes improved cryptomelane activity by increasing the available

630 surface active sites and more accessible pore channels for adsorption and desorption of HCHO

631 molecules and reaction products respectively (*36*). Sekine (*2*) showed that fine MnO_2 catalysts

632 with higher specific surface area (163 m^2/g) achieved higher HCHO oxidation compared to MnO_2

633 catalysts with a specific surface area of 61 m^2/g. Similarly, Tian et al. (54) also reported that

634 birnessite structured manganese catalysts having higher specific surface area exhibited better

635 catalytic activities compared to those with lower specific surface areas.

636 However, high specific surface area does not always translate into superior catalytic activities in

637 HCHO oxidation reactions. The activity of birnessite-type MnO_2 was shown to be independent on

638 the catalysts' specific surface area trend (*74*) but on the relative content of surface adsorbed oxygen

639 species and the manganese oxidation state. The catalyst with the highest manganese vacancy had

640 the lowest specific surface area but exhibited the best catalytic activity. Shi et al. (*95*) also

641 demonstrated that the activity trend of Co-Mn oxides composite with varying Co/Mn molar ratios

642 did not follow their specific surface area trend, and in fact the catalysts with the smallest specific

643 surface area exhibited the best catalytic activity. Complete oxidation of HCHO was achieved at

644 75°C on Co-Mn oxides (molar ratio: 3/1) with specific surface area of 92 m^2/g while only 64%

645 conversion was attained on Co-Mn oxides (molar ratio: 2/1) with specific surface area of 172 m^2/g

646 at the same reaction temperature. The higher activity of Co-Mn (3/1) oxides was a result of increase

647 in the relative amount of surface adsorbed oxygen species realized from the creation of solid

648 solution by the incorporation of Mn into the lattice structure of Co_3O_4. Fan et al. (*67*) also showed

649 that Co_3O_4 catalysts with high surface content of K^+, CO_3^{2-} and Co^{3+} exhibited better activity

650 despite having relatively smaller specific surface area.

5. Effect of reaction conditions on HCHO oxidation efficiency

Reaction parameters for HCHO oxidation process such as temperature, relative humidity, reactants' space velocity and HCHO concentration play great roles in ensuring the overall effectiveness of the oxidation reaction. These parameters need to be optimized especially reaction temperature considering the potential application of the process (no harmful by-products generation), in order to realize practically effective HCHO oxidation.

5.1 Reaction temperature and time

Reaction temperature is critical in HCHO oxidation, and generally the efficiency of HCHO oxidation over catalyst improves with increasing temperature even though some highly active catalysts are able to achieve complete oxidation at room temperature. Most of the reported transition metal based catalysts attained complete HCHO oxidation at temperatures above 100°C (*21,36,55,67,73,82*) with very few below 100 °C (*19,21,73,87,95,98*). Figure 6 presents the conversion/removal efficiency of HCHO as a function of reaction temperatures over different catalysts. However, it does not provide a basis for comparison due to the differences in the initial HCHO concentration and feed flow rate employed in various experiments. This makes it difficult to evaluate the specific reaction rates (equation 1) (*74*) of variously reported catalysts for rational comparison. For static systems, experiments are normally conducted at room temperature; in which case HCHO oxidation becomes a function of time in addition to other factors catalyst based factors discussed earlier (section 4). Figure 7 presents HCHO removal efficiency over various catalysts as a function of reaction time. It can be seen in Figure 7 that long reaction time is required to achieve complete HCHO removal in static system. For proper comparison, other factors such as initial HCHO concentration and the mass of catalyst used should be taken into account.

673 In view of these, more investigations are required to improve the activity of transition metal based

674 catalysts at low temperature in order to compete with noble metal based catalysts which could

675 successfully oxidize HCHO even at room temperature (*48,101*).

676 $$specific\ reaction\ rates\ \left(\frac{\mu mol}{m^2.min}\right) = \frac{C_{HCHO} \div 22.4 \times F \times \eta}{S_{BET} \times m} \ \dots\dots\dots\dots\dots\dots\dots\dots\ (1)$$

677 Where C_{HCHO} is the inlet HCHO concentration (ppm), F is the flow rate (ml/min), η is the

678 percentage HCHO conversion (CO_2 generation), S_{BET} catalysts specific surface area and m is the

679 catalyst mass.

680 5.2 Relative humidity

681 Relative humidity (RH) at moderate levels influences the efficiency of HCHO oxidation, however

682 at higher RH competitive adsorption of H_2O molecules tend to block the catalyst's active surface

683 hence impinging activity. RH also helps in replenishing the supply of surface active hydroxyl

684 groups which are consumed during HCHO oxidation, via the reaction of H_2O vapor and surface

685 active oxygen (O_2^-, O^-) (*73,102*). Wang et al. (*18*) noted that in the presence of 50% RH, H_2O

686 vapor react with surface active oxygen to generate enough surface hydroxyl groups to sustain

687 HCHO oxidation reaction at RT. H_2O vapor also helps in carbonates desorption from the catalyst's

688 surface via competitive adsorption, thereby enabling recovery of catalytic activity (*73*). Wang et

689 al. (*73*) indicated that RH in the range of 33% to 65% enhanced HCHO removal on birnessite

690 structured manganese at room temperature. However at higher RH (92%), catalytic activity was

691 impacted owing to competitive adsorption of H_2O molecules on the catalyst's surface. Similar

692 effects were observed with MnO_2/PET (*18*): at 0% RH significant deactivation was observed due

693 to the formation of formate species on the catalyst's surface; however at higher RH (50%), the

694 catalyst remained active and stable while activity significantly dropped when the RH was further

695   raised to 80% due to competitive adsorption of H_2O molecules. This conforms to the findings of

696   Sidheswaran et al. (*97*).

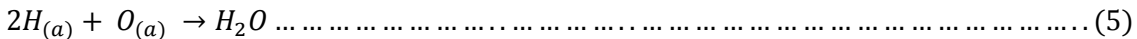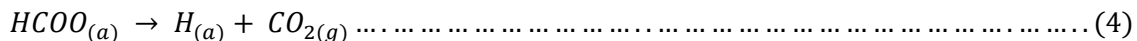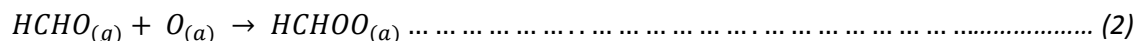697   5.3 Feed flow rate and feed concentration

698   The significance of feed (reactants) flow rate in terms of gas hourly space velocity (GHSV) on

699   catalytic oxidation of HCHO was also reported in the literature. GHSV can improve the efficiency

700   of a fixed bed reaction system in two ways; at higher velocity, it will help to a certain extent in

701   enhancing external mass transfer while at a lower velocity it increases the residence time of

702   reactants in the reactor (*52*). It was however reported that the efficiency of HCHO oxidation

703   reactions decreases with increasing space velocity (*39,69,70,101*) and vice-versa.   In view of

704   these, it could be insinuated that external mass transfer has little or no limitation on the efficiency

705   of HCHO oxidation reaction, although an experimental evaluation on external mass transfer effect

706   would be required.

707   In addition, HCHO feed concentration is another significant parameter for HCHO oxidation

708   process. HCHO oxidation efficiency tends to decrease with an increase in the feed concentration.

709   Chuang et al. (*28*) demonstrated that an increase in HCHO feed concentration led to a decrease in

710   conversion at the same reaction temperature. Likewise, Tang et al. (*48*) reported that catalytic

711   activity decreased with rise in HCHO feed concentration from 30 to 580 ppm and that the catalysts

712   were more active and stable at lower concentration. Correspondingly, Li et al. (*98*) pointed out that

713   MnO_2/AC completely lost its activity when exposed to 5 mg/m^3 HCHO feed concentration in 32

714   hrs, compared to its sustained HCHO oxidation efficiency of up to 70% for 80 hrs under a HCHO

715   feed concentration of 0.5 mg/m^3.

6. Reaction mechanism of catalytic oxidation of HCHO

Understanding the reaction mechanism of HCHO oxidation over transition metal based catalysts is vital for the development of catalysts with high efficiency, low cost and good stability. Different catalysts for HCHO oxidation may exhibit varying reaction mechanisms because different intermediate species could be formed with various active oxygen species and surface active sites (*4*). Oxidation reaction of HCHO over some transition metals based catalysts were shown to conform to Mars-van Krevelen mechanism (*18,19,97*). In this mechanism, reaction proceeds via a two-stage redox reaction with an assumption of constant surface oxygen. The catalyst's surface is first oxidized by gas phase molecular oxygen to form surface adsorbed oxygen species which subsequently reduces the pollutant (*52*).

Sekine (*2*) proposed that HCHO oxidation on metal oxides catalysts proceeds first by adsorption on the catalyst's surface followed by decomposition through the formation of formate intermediates on the surface, then the intermediates are subsequently decomposed to H_2O and CO_2 as presented in equations (2-5) where *g* and *a* indicate gaseous phase and adsorbed species, respectively.

$$HCHO_{(g)} + O_{(a)} \rightarrow HCHOO_{(a)} \dots\dots\dots\dots\dots\dots\dots\dots\dots\dots\dots\dots\dots\dots\dots\dots\dots\dots \textit{(2)}$$

$$HCHOO_{(a)} \rightarrow HCOO_{(a)} + H_{(a)} \dots\dots\dots\dots\dots\dots\dots\dots\dots\dots\dots\dots\dots\dots\dots\dots (3)$$

$$HCOO_{(a)} \rightarrow H_{(a)} + CO_{2(g)} \dots\dots\dots\dots\dots\dots\dots\dots\dots\dots\dots\dots\dots\dots\dots\dots\dots (4)$$

$$2H_{(a)} + O_{(a)} \rightarrow H_2O \dots\dots\dots\dots\dots\dots\dots\dots\dots\dots\dots\dots\dots\dots\dots\dots\dots\dots\dots (5)$$

Tang et al. (*86*) indicated the oxidation of HCHO over MnO_x-CeO_2 catalyst was attained through the effective transfer of oxygen species from CeO_2 oxygen reservoir to MnO_2 active state. This synergy is achieved through the effective activation of feed molecular oxygen and the transfer of

738   the activated oxygen to replace the released active oxygen species from MnO_2 which participated

739   in HCHO oxidation through a series of redox cycles involving Mn^{4+}/Mn^{3+} and Ce^{4+}/Ce^{3+} (*48,86*)

740   as shown in Figure 8.

741   Wang et al. (*73*) proposed three-step mechanism for HCHO oxidation on birnessite structured

742   manganese catalyst at room temperature as presented in Figure 9. The reaction first proceeds

743   through H-bond between HCHO molecules and birnessite bonded H_2O molecules. The adsorbed

744   molecules are then oxidized to formate and carbonates by structural hydroxyl species.

745   Subsequently, the consumed hydroxyl ions are replaced through the reaction between surface

746   active oxygen and H_2O molecules. An oxygen vacancy is then formed on the site of the consumed

747   surface active oxygen species, which further acts as a site for molecular oxygen activation to active

748   species for continuous reaction (*74*). Wang et al. (*68*) reported that only hydrocarbonate species

749   were observed on the surface of 3D-Co-Mn catalysts with no obvious formation of formate species,

750   probably due to the fast conversion rate of formate to hydrocarbonates on the catalyst's surface as

751   suggested by the authors. The hydrocarbonate species were totally decomposed at 70°C as reported

752   by Shi et al. (*95*) for Co-Mn.

753   Shi et al. (*95*) indicated that the mechanism of HCHO oxidation over Co-Mn oxides proceeds via

754   the formation of DOM and formate species as intermediates. During adsorption process, HCHO is

755   immediately converted to DOM as no HCHO molecules were observed on the catalyst surface at

756   room temperature. The active DOM species react with surface adsorbed oxygen species to form

757   formate species and part of them are further oxidized to hydrocarbonates. At higher temperature

758   (50°C), further oxidation of formate and degradation of hydrocarbonate species occur. At the

759   complete oxidation temperature of HCHO (75°C), only adsorbed H_2O molecules were observed,

760   indicating complete oxidation of all the intermediate species. Hence, formate oxidation and

761 hydrocarbonate decomposition are considered as the rate-limiting steps for HCHO oxidation over

762 Co-Mn oxides catalyst.

763 A reaction mechanism for 2D ordered mesoporous Co_3O_4, Au/Co_3O_4 and $Au/Co_3O_4\text{-}CeO_2$ at room

764 temperature had been proposed by Ma et al. (*51*) as depicted in Figure 10. In this mechanism,

765 formate species are first generated by the nucleophilic attack on the C-H in HCHO by surface

766 active oxygen on the (110) facet of Co_3O_4 (with Co^{3+} as the active state). The formate species are

767 further oxidized to bicarbonates by surface active oxygen species. Carbonic acid species are then

768 generated by the reaction of the bicarbonates and H^+, which are subsequently decomposed to CO_2.

769 In contrast, Fan et al. (*67*) indicated that hydroxyl groups were responsible for the immediate

770 oxidation of HCHO on the surface of Co_3O_4 and that DOM and formate species were observed as

771 the intermediates during the adsorption of HCHO on the catalyst's surface as previously reported

772 (*95*). However, the behavior of the catalysts at elevated temperature in the presence of O_2 was

773 influenced by the existence of K^+ ions on the catalyst's surface. In the presence of K^+ ions, DOM

774 species generated during the adsorption process are converted to formate species and formate

775 oxidation to bicarbonates becomes the key reaction step. It was proposed that hydroxyl groups

776 were generated from surface hydrolysis of K_2CO_3 and got consumed during the reaction. The

777 consumed hydroxyl groups were replenished by the H_2O molecules generated thus K_2CO_3 surface

778 hydrolysis was sustained and the reaction was accelerated. On the other hand, in the absence of

779 K_2CO_3 at elevated temperature (80°C) only few DOM species could be converted to formate

780 species due to the lack of hydroxyl groups on the surface of Co_3O_4, thus formate decomposition to

781 carbonates and bicarbonates became the key reaction step at $\geq 80°C$. Here it could be observed

782 that the existence of K^+ on the surface of Co_3O_4 changed the reaction path from formate

783 decomposition to formate oxidation and continued supply of surface hydroxyl group necessary for

784 the oxidation reaction was sustained by K_2CO_3 surface hydrolysis thus promoting HCHO

785 oxidation. Similar promotion effects of K^+ was observed for Ag/Co_3O_4 (*46*), Na^+ for ceramic

786 honeycombs (*103*) and Na^+ for Pd/TiO_2 (*59*).

787 Lu et al. (*87*) proposed a reaction pathway for HCHO over graphene-MnO_2 hybrid catalysts. In

788 this mechanism, HCHO is first oxidized to form formate intermediates while molecular oxygen is

789 activated and transferred to active Mn sites through Mn^{4+}/Mn^{3+} redox cycle. Graphene being an

790 electrical conductor reduces electron transfer resistance and enhances the rate of charge transfer

791 between Mn^{4+} and Mn^{3+}, thereby improving the overall efficiency of the process. Thereafter, due

792 to the abundant amount of surface hydroxyl groups on the hybrid catalyst, formate species were

793 directly converted to CO_2 and H_2O, while the consumed hydroxyl ions were regenerated by the

794 produced H_2O molecules as reported by other authors (*67*).

795 The reaction mechanism of HCHO catalytic oxidation is intricate and varies with the type and

796 amount of surface active oxygen or hydroxyl species present. But generally, formate species are

797 key intermediates present on almost all transition metal based catalysts. Other species such as

798 DOM and hydrocarbonates are also reported as intermediates for HCHO oxidation. However, the

799 reported pathways for HCHO decomposition varied in the literature. In some mechanisms DOM

800 species are first generated followed by their conversion to formate intermediates, which are

801 subsequently oxidized to hydrocarbonates and finally CO_2 and H_2O molecules are generated by

802 hydrocarbonate decomposition. In other mechanisms, no DOM species are observed and formates

803 are directly oxidized to CO_2 and H_2O especially in the presence of high amount of surface hydroxyl

804 groups (*67,87*). The reaction mechanism of transition metal based catalysts for HCHO oxidation

805 is minimally reported in the literature. This prompts the need for further elaborate investigation

806 into the mechanism on various active transition metals especially as it relates to the surface

807 properties of these catalysts, and the specific role of hydroxyl and oxygen species and the

808 promotional effects of alkali metals (Na^+, K^+) on the overall efficiency of the reaction. This will

809 provide more information and offer the basis for the design of yet more active and cost-effective

810 catalysts for practical application.

811 **7. Conclusions and outlook**

812 Formaldehyde is one of the most harmful indoor air pollutants as it has adverse effects on human

813 health due to its toxicity and carcinogenicity. Techniques such as adsorption, photo-catalytic

814 oxidation and catalytic oxidation have been used in HCHO removal. Adsorption removal is limited

815 by the adsorption capacity of the adsorbents deployed and the hazard of HCHO desorption during

816 regeneration while photo-catalytic oxidation produces hazardous by-products. Catalytic oxidation

817 offsets these drawbacks and can achieve complete conversion of HCHO into CO_2 and H_2O

818 molecules without the formation of hazardous by-products.

819 Noble metal based catalysts exhibit excellent low and even room temperature HCHO oxidation

820 capabilities but their practical application is restricted by their cost and availability. Recent

821 investigations focus on the use of relatively cheap and abundant transition metals oxides and

822 improving their low temperature performance. More attention has mainly been focused on the

823 improvement and exploitation of various structures and morphologies of manganese oxide

824 catalysts due to its high activity yet with little attention on other transition metal catalysts. As such,

825 more investigation needs to be done on the improvement of morphological structures, textural and

826 redox properties of these materials.

827 For practical air purification application in air purifiers or building HVAC systems, substrate

828 materials with low air resistance and pressure drop are required to immobilize catalysts to avoid

829   dust contamination and catalysts leaching into treated air stream. However, only a few substrate

830   materials have been reported in the literature and hence the need for further evaluation of more

831   materials to understand their interactions with the catalysts and effect on activity for pragmatic air

832   purification process. In addition to the development of these materials, they need to be tested under

833   real indoor environmental conditions in air purifiers to evaluate the effects of system conditions

834   such as face velocity, dust particle contamination and particle leaching on the efficiency and

835   stability of the catalysts.

836   No single property is decisive for catalytic performance of transition metal oxides for complete

837   oxidation of HCHO but a combination of several factors which include specific surface area, metal

838   oxidation state, adsorbed and surface oxygen species, structure and morphology of the catalyst.

839   Improvement of the morphological structures of transition metal based catalysts relative to their

840   conventional bulk counterparts enhances their catalytic activity through improvement of specific

841   surface area, mesoporosity and exposure of surface active metals and oxygen species. The tunnel

842   structure of catalysts enhances the rate of adsorption of HCHO onto the active sites for

843   decomposition and the rate of product desorption from the sites to make them available for the

844   next molecules. This is particularly promoted when the catalyst's effective diameter is close to the

845   dynamic diameter of HCHO (*55*). Oxidation state of metals in the catalyst is also vital for

846   determining activity and higher oxidation states seem to be more active; Mn^{4+} in the case of

847   manganese and Co^{3+} in the case of cobalt were identified to be the most active states for HCHO

848   activation.   Several methods have been proposed for improving the oxidation sate of metal oxides

849   which include modified synthesis, controlling calcination temperature and the relative molar ratio

850   of component elements, to maintain solid solution stability in the case of composite catalysts (86).

851 The use of hard template materials has been proven effective in providing the plane structure for

852 improved exposure of more surface active sites and enhanced access to these sites.

853 Active surface oxygen and hydroxyl species directly participate in oxidizing HCHO molecules

854 and all other intermediate species into CO_2 and H_2O. The higher the concentration of these active

855 materials on the catalyst's surface the better its HCHO oxidative activity. The availability of

856 surface active oxygen species and the rate of molecular oxygen activation could be enhanced by

857 the formation of surface vacancy using dopants and formation of solid solution composites with

858 oxygen carrier materials. Recently reported works (*80,81*) indicated that creating oxygen surface

859 vacancy using dopants increases the activation rate of molecular oxygen to more active and

860 reactive oxygen species thereby providing more abundant oxygen species for HCHO oxidation.

861 However not much has been reported on surface vacancy creation and surface modification using

862 dopants on transition metal based catalyst for HCHO oxidation, thereby prompting the need for

863 further exploration. The use of oxygen carrier materials for composite formation on the other hand

864 improves the transfer rate of active oxygen from the rich oxygen sources of the carrier to the active

865 metal sites in a complete redox cycle. The formation of solid solution within the solubility limit of

866 the composite is critical to achieving synergistic effects either through oxygen transfer or oxygen

867 vacancy creation, above which phase segregation occurs and synergy is lost. Most of the reported

868 composites in the literature for HCHO oxidation focus on the use of CeO_2 as composite material

869 with little or no attention to other oxygen carriers.

870 Furthermore, enhancing the electrical conductivity of catalyst through the formation of hybrids or

871 composites with electrically conducting materials such as graphene (*87*) was shown to greatly

872 improve catalytic activity at low temperature. The hybrid system exposed more Mn^{4+} active sites,

873 enhanced charge transport during Mn redox cycle and offered higher content of surface hydroxyl

874   species, which eases HCHO oxidation and improves the catalyst's activity at low temperature.

875   However, very few studies have been reported for catalyst's electrical conductivity enhancement

876   using conductor materials for HCHO oxidation. Hence further investigation into the influence of

877   dopants and other conductor materials on the activity of transition metals based catalysts for

878   improved low temperature HCHO oxidation will be desirable. In addition to catalytic properties,

879   reaction parameters such as reaction temperature, relative humidity, space velocity and HCHO

880   feed concentration also affect the overall efficiency of HCHO oxidation. Relative humidity at

881   moderate levels helps in enhancing the availability of surface active hydroxyl groups via the

882   reaction of H_2O vapor and surface active oxygen but becomes detrimental at higher levels.

883   The reaction mechanism of HCHO is complex and depends on the type of catalysts, the oxidation

884   state and amount of active metals and the nature of surface active oxygen (adsorbed and or lattice)

885   present. Although further research is required to ascertain the respective role of each in HCHO

886   oxidation. Only a few mechanisms were reported for transition metal catalysts, as such further

887   investigation is required into the reaction mechanism especially as it relates to the catalyst's surface

888   properties and the role of surface active oxygen or hydroxyl species. But generally, formate

889   species, DOM and hydrocarbonates are the identified intermediates for HCHO oxidation on

890   transition metal based catalysts. However, the reported pathways for HCHO decomposition varied

891   in the literature. In some mechanisms DOM species are first generated followed by DOM

892   conversion to formate intermediates, which are subsequently oxidized to hydrocarbonates and

893   finally CO_2 and H_2O molecules are generated by hydrocarbonate decomposition. In other

894   mechanisms, no DOM species are observed and formates are directly oxidized to CO_2 and H_2O

895   molecules without the formation of hydrocarbonates especially in the presence of high amount of

896   surface hydroxyl groups.

Acronyms

1D	One Dimensional
2D	Two Dimensional
3D	Three Dimensional
3DOM	Three Dimensional Ordered Macroporous
AC	Activated Carbon
CTAB	Cetyltrimethylammonium Bromide
DOM	Dioxymethylene
GHSV	Gas Hourly Space Velocity
HCHO	Formaldehyde
HVAC	Heating Ventilation and Air Conditioning
IARC	International Agency for Research on Cancer
KIT-6	Korea Advanced Institute of Science and Technology-6
K-OMS-2	Potassium-Octahedral Molecular Seive-2
PET	Polyethylene Terephthalate
R	Specific Reaction Rate
Redox	Reduction-Oxidation
RH	Relative humidity
SBA-15	Santa Barbara Amorphous-15
TOF	Turnover Frequency
VOC	Volatile Organic Compounds
WHO	World Health Organization

Acknowledgement

42

References

928   (1)   Maddalena, R.; Russell, M.; Sullivan, D.P.; Apte, M.G. Formaldehyde and Other Volatile
929   Organic Chemical Emissions in Four FEMA Temporary Housing Units. *Environ. Sci. Technol.*
930   **2009,** *43* (15), 5626-5632.
931
932   (2)   Sekine, Y. Oxidative decomposition of formaldehyde by metal oxides at room temperature.
933   *Atmos. Environ.* **2002,** *36* (35), 5543-5547.
934
935   (3)   Salthammer, T.; Mentese, S.; Marutzky, R. Formaldehyde in the Indoor Environment. *Chem. Rev.*
936   **2010,** *110* (4), 2536-2572.
937
938   (4)   Bai, B.; Qiao, Q.; Li, J.; Hao, J. Progress in research on catalysts for catalytic oxidation of
939   formaldehyde. *Chin. J. Catal.* **2016,** *37* (1), 102-122.
940
941   (5)   Sekine, Y.; Nishimura, A. Removal of formaldehyde from indoor air by passive type air-cleaning
942   materials. *Atmos. Environ.* **2001,** *35* (11), 2001-2007.
943
944   (6)   International Agency for Cancer Research (IACR*)* working group on the identification of
945   Carcinogenic Risks to Humans. *Formaldehyde, 2-Butoxyethanol and 1-tert-Butoxypropan-2-ol.*
946   WHO; Lyon France, 2006**;** volume 88.
947
948   (7)   World Health Organization. *WHO guidelines for indoor air quality: selected pollutants*; WHO:
949   Copenhegan, 2010.
950
951   (8)   Le, Y.; Guo, D.; Cheng, B.; Yu, J. Bio-template-assisted synthesis of hierarchically hollow SiO 2
952   microtubes and their enhanced formaldehyde adsorption performance. *Appl. Surf. Sci.* **2013,** *274*,
953   110-116.
954
955   (9)   Chen, D.; Qu, Z.; Sun, Y.; Wang, Y. Adsorption–desorption behavior of gaseous formaldehyde
956   on different porous Al2O3 materials. *Colloids Surf., A* **2014,** *441* 433-440.
957
958   (10)   Ma, C.; Li, X.; Zhu, T. Removal of low-concentration formaldehyde in air by adsorption on
959   activated carbon modified by hexamethylene diamine. *Carbon* **2011,** *49* (8), 2873-2875.
960
961   (11)   Rezaee, A.; Rangkooy, H.; Jonidi-Jafari, A.; Khavanin, A. Surface modification of bone char for
962   removal of formaldehyde from air. *Appl. Surf. Sci.* **2013,** *286*, 235-239.
963
964   (12)   Lu, Y.; Wang, D.; Ma, C.; Yang, H. The effect of activated carbon adsorption on the
965   photocatalytic removal of formaldehyde. *Build. Environ.* **2010,** *45* (3), 615-621.
966
967   (13)   Tong, H.; Zhao, L.; Li, D.; Zhang, X. N, Fe and WO3 modified TiO$_2$ for degradation of
968   formaldehyde. *J. Alloys Compd.* **2011,** *509* (22), 6408-6413.
969
970   (14)   Fu, P.; Zhang, P.; Li, J. Photocatalytic degradation of low concentration formaldehyde and
971   simultaneous elimination of ozone by-product using palladium modified TiO 2 films under UV
972   254+ 185nm irradiation. *Appl. Catal., B* **2011,** *105* (1), 220-228.
973
974   (15)   Liang, W.; Li, J.; Jin, Y. Photo-catalytic degradation of gaseous formaldehyde by TiO 2/UV,
975   Ag/TiO 2/UV and Ce/TiO 2/UV. *Build. Environ.* **2012,** *51*, 345.-350

976   (16)   Ghosh, J.P.; Sui, R.; Langford, C.H.; Achari, G.; Berlinguette, C.P. A comparison of several
977   nanoscale photocatalysts in the degradation of a common pollutant using LEDs and conventional
978   UV light. *Water Res.* **2009,** *43* (18), 4499-4506.
979

980   (17)   Shie, J.L.; Lee, C.H.; Chiou, C.S.; Chang, C.T.; Chang, C.C.; Chang, C.Y. Photodegradation
981   kinetics of formaldehyde using light sources of UVA, UVC and UVLED in the presence of
982   composed silver titanium oxide photocatalyst. *J. Hazard. Mater.* **2008,** *155* (1), 164-172.
983

984   (18)   Wang, J.; Yunus, R.; Li, J.; Li, P.; Zhang, P.; Kim, J. In situ synthesis of manganese oxides on
985   polyester fiber for formaldehyde decomposition at room temperature. *Appl. Surf. Sci.* **2015,** *357*,
986   787-794.
987

988   (19)   Zhang, J.; Li, Y.; Wang, L.; Zhang, C.; He, H. Catalytic oxidation of formaldehyde over
989   manganese oxides with different crystal structures. *Catal. Sci. Technol.* **2015,** *5* (4), 2305-2313.
990

991   (20)   Luengas, A.; Barona, A.; Hort, C.; Gallastegui, G.; Platel, V.; Elias, A.   A review of indoor air
992   treatment technologies. *Rev. Environ. Sci. Bio/Technol.* **2015,** *14* (3), 499-522.
993

994   (21)   Chen, H.; He, J.; Zhang, C.; He, H. Self-assembly of novel mesoporous manganese oxide
995   nanostructures and their application in oxidative decomposition of formaldehyde. *J. Phys. Chem.*
996   *C* **2007,** *111* (49), 18033-18038.
997

998   (22)   Zhang, C.; He, H. A comparative study of TiO 2 supported noble metal catalysts for the oxidation
999   of formaldehyde at room temperature. *Catal. Today* **2007,** *126* (3), 345-350.
1000

1001   (23)   Zhang, C.; Liu, F.; Zhai, Y.; Ariga, H.; Yi, N.; Liu, Y.; Asakura, K.; Flytzani‐Stephanopoulos,
1002   M.; He, H. Alkali   Metal   Promoted Pt/TiO2 Opens a More Efficient Pathway to Formaldehyde
1003   Oxidation at Ambient Temperatures. *Angew. Chem., Int. Ed.* **2012,** *51* (38), 9628-9632.
1004

1005   (24)   Huang, H.; Leung, D.Y. Complete elimination of indoor formaldehyde over supported Pt
1006   catalysts with extremely low Pt content at ambient temperature. *J. Catal.* **2011,** *280* (1), 60-67.
1007

1008   (25)   Kim, S.S.; Park, K.H.; Hong, S.C. A study on HCHO oxidation characteristics at room
1009   temperature using a Pt/TiO 2 catalyst. *Appl. Catal., A* **2011,** *398* (1), 96-103.
1010

1011   (26)   Yan, Z.; Xu, Z.; Yu, J.; Jaroniec, M. Enhanced formaldehyde oxidation on CeO 2/AlOOH-
1012   supported Pt catalyst at room temperature. *Appl. Catal., B* **2016,** *199*, 458-465.
1013

1014   (27)   Nie, L.; Jiaguo, Y.; Xinyang, L.; Bei, C.; Gang, L.; Mietek, J. Enhanced performance of NaOH-
1015   modified Pt/TiO2 toward room temperature selective oxidation of formaldehyde. *Environ. Sci.*
1016   *Technol.* **2013,** *47* (6), 2777-2783.
1017

1018   (28)   Chuang, K.T.; Zhou, B.; Tong, S. Kinetics and Mechanism of Catalytic Oxidation of
1019   Formaldehyde over Hydrophobic Catalysts. *Ind. Eng. Chem. Res.* **1994,** *33* (7), 1680-1686.
1020

1021   (29)   An, N.; Zhang, W.; Yuan, X.; Pan, B.; Liu, G.; Jia, M.; Yan, W.; Zhang, W. Catalytic oxidation
1022   of formaldehyde over different silica supported platinum catalysts. *Chem. Eng. J. (Amsterdam,*
1023   *Neth.)* **2013,** *215*, 1-6.
1024

1025 (30) Peng, J.; Wang, S. Performance and characterization of supported metal catalysts for complete
1026   oxidation of formaldehyde at low temperatures. *Appl. Catal., B* **2007,** *73* (3), 282.
1027

1028 (31) Park, S.J.; Bae, I.; Nam, I.S.; Cho, B.K.; Jung, S.M.; Lee, J.H. Oxidation of formaldehyde over
1029   Pd/Beta catalyst. *Chem. Eng. J. (Amsterdam, Neth.)* **2012,** *195*, 392-402.
1030

1031 (32) de la Peña O'Shea, V. A.; Alvarex-Galvan, M.C; Fierro, J.L.; Arias, P. L. Influence of feed
1032   composition on the activity of Mn and PdMn/Al$_2$O$_3$ catalysts for combustion of
1033   formaldehyde/methanol. *Appl. Catal., B* **2005,** *57* (3), 191-199.
1034

1035 (33) Huang, H.; Leung, D.Y. Complete Oxidation of Formaldehyde at Room Temperature Using TiO$_2$
1036   Supported Metallic Pd Nanoparticles. *ACS Catal.* **2011,** *1* (4), 348-354.
1037 .

1038 (34) Mao, C.F.; Vannice, M. A. Formaldehyde Oxidation Over Ag Catalysts. *J. Catal.* **1995,** *154* (2),
1039   230-244.
1040

1041 (35) Qu, Z.; Shen,S.; Chen, D.; Wang, Y. Highly active Ag/SBA-15 catalyst using post-grafting
1042   method for formaldehyde oxidation. *J. Mol. Catal. A: Chem.* **2012,** *356*, 171-177.
1043

1044 (36) Tian, H.; He, J.; Liu, L.; Wang, D. Effects of textural parameters and noble metal loading on the
1045   catalytic activity of cryptomelane-type manganese oxides for formaldehyde oxidation. *Ceram.*
1046   *Int.* **2013,** *129* (1), 315-321.
1047

1048 (37) Li, H. F.; Zhang, N.; Chen, P.; Luo, M. F.; Lu, J. Q. High surface area Au/CeO$_2$ catalysts for low
1049   temperature formaldehyde oxidation. *Appl. Catal., B* **2011,** *110*, 279-285.
1050

1051 (38) Imamura, S.; Uchihori, D.; Utani, K.; Ito, T. Oxidative decomposition of formaldehyde on silver-
1052   cerium composite oxide catalyst *Catal. Lett.* **1994,** *24* (3-4), 377-384.
1053

1054 (39) An, N.; Yu, Q.; Liu, G.; Li, S.; Jia, M.; Zhang, W. Complete oxidation of formaldehyde at
1055   ambient temperature over supported Pt/Fe$_2$O$_3$ catalysts prepared by colloid-deposition method. *J.*
1056   *Hazard. Mater.* **2011,** *186* (2), 1392-1397.
1057

1058 (40) Shen, Y.; Yang, X.; Wang, Y.; Zhang, Y.; Zhu, H.; Gao, L.; Jia, M. The states of gold species in
1059   CeO$_2$ supported gold catalyst for formaldehyde oxidation. *Appl. Catal., B* **2008,** *79* (2), 142-148.
1060

1061 (41) Yu, X.; He, J.; Wang, D.; Hu, Y.; Tian, H.; He, Z. Facile Controlled Synthesis of Pt/MnO$_2$
1062   Nanostructured Catalysts and Their Catalytic Performance for Oxidative Decomposition of
1063   Formaldehyde. *J. Phys. Chem. C* **2011,** *116* (1), 851-860.
1064

1065 (42) Hu, P.; Amghouz, Z.; Huang, Z.; Xu, F.; Chen, Y.; Tang, X. Surface-Confined Atomic Silver
1066   Centers Catalyzing Formaldehyde Oxidation. *Environ. Sci. Technol.* **2015,** *49* (4), 2384-2390.
1067

1068 (43) Bai, B.; Qiao, Q.; Arandiyan, H.; Li, J.; Hao, J. Three-Dimensional Ordered Mesoporous MnO$_2$-
1069   Supported Ag Nanoparticles for Catalytic Removal of Formaldehyde. *Environ. Sci. Technol.*
1070   **2016,** *50* (5), 2635-2640.
1071

1072 (44) Zhang, J.; Jin, Y.; Li, C.; Shen, Y.; Han, L.; Hu, Z.; Di, X.; Liu, Z. Creation of three-
1073   dimensionally ordered macroporous Au/CeO$_2$ catalysts with controlled pore sizes and their
1074   enhanced catalytic performance for formaldehyde oxidation. *Appl. Catal., B* **2009,** *91* (1), 11-20.

1075   (45)   Wang, R.; Li, J. OMS-2 Catalysts For Formaldehyde Oxidation: Effects of Ce And Pt on
1076   Structure And Performance of the Catalysts. *Catal. Lett.* **2009,** *131* (3-4), 500-505.

1077

1078   (46)   Bai, B.; Li, J. Positive Effects of K+ Ions on Three-Dimensional Mesoporous Ag/Co$_3$O$_4$ Catalyst
1079   For HCHO Oxidation. *ACS Catal.* **2014,** *4* (8), 2753-2762.

1080

1081   (47)   Ma, L.; Wang, D.; Li, J.; Bai, B.; Fu, L.; Li, Y. Ag/CeO$_2$ nanospheres: Efficient catalysts for
1082   formaldehyde oxidation. *Appl. Catal., B* **2014,** *148*, 36-43.

1083

1084   (48)   Tang, X.; Chen, J.; Huang, X.; Xu, Y.; Shen, W. Pt/MnO$_x$–CeO$_2$ catalysts for the complete
1085   oxidation of formaldehyde at ambient temperature. *Appl. Catal., B* **2008,** *81* (1), 115-121.

1086

1087   (49)   Tang, X.; Chen, J.; Li, Y.; Li, Y.; Xu, Y.; Shen, W. Complete oxidation of formaldehyde over
1088   Ag/MnO$_x$–CeO$_2$ catalysts. *Chem. Eng. J. (Amsterdam, Neth.)* **2006,** *118* (1), 119-125.

1089

1090   (50)   Liu, B.; Liu, Y.; Li, C.; Hu, W.; Jing, P.; Wang, Q.; Zhang, J. Three-dimensionally ordered
1091   macroporous Au/CeO$_2$-Co$_3$O$_4$ catalysts with nanoporous walls for enhanced catalytic oxidation of
1092   formaldehyde. *Appl. Catal., B* **2012,** *127*, 47-58.

1093

1094   (51)   Ma, C.; Wang, D.; Xue, W.; Dou, B.; Wang, H.; Hao, Z. Investigation of Formaldehyde
1095   Oxidation over Co$_3$O$_4$−CeO$_2$ and Au/Co$_3$O$_4$−CeO$_2$ Catalysts at Room Temperature: Effective
1096   Removal and Determination of Reaction Mechanism. *Environ. Sci. Technol.* **2011,** *45* (8), 3628-
1097   3634.

1098

1099   (52)   Pei, J.; Zhang, J.S. Critical review of catalytic oxidization and chemisorption methods for indoor
1100   formaldehyde removal. *HVACR Res.* **2011,** *17* (4), 476-503.

1101

1102   (53)   Quiroz, J.; Giraudon, J.M.; Gervasini, A.; Dujardin, C.; Lancelot, C.; Trentesaux, M.; Lamonier,
1103   J.F. Total Oxidation of Formaldehyde over MnO$_x$-CeO$_2$ Catalysts: The Effect of Acid Treatment.
1104   *ACS Catal.* **2015,** *5* (4), 2260-2269.

1105

1106   (54)   Tian, H.; He, J.; Liu, L.; Wang, D.; Hao, Z.; Ma, C. Highly active manganese oxide catalysts for
1107   low-temperature oxidation of formaldehyde. *Microporous Mesoporous Mater.* **2012,** *151*, 397-
1108   402.

1109

1110   (55)   Chen, T.; Dou, H.; Li, X.; Tang, X.; Li, J.; Hao, J. Tunnel structure effect of manganese oxides in
1111   complete oxidation of formaldehyde. *Microporous Mesoporous Mater.* **2009,** *122* (1), 270-274.

1112

1113   (56)   Tian, H.; He, J.; Zhang, X.; Zhou, L.; Wang, D. Facile synthesis of porous manganese oxide K-
1114   OMS-2 materials and their catalytic activity for formaldehyde oxidation. *Microporous*
1115   *Mesoporous Mater.* **2011,** *138* (1), 118-122.

1116

1117   (57)   Tasbihi, M.; Bendyna, J. K.; Notten, P. H. A Short Review on Photocatalytic Degradation of
1118   Formaldehyde. *J. Nanosci. Nanotechnol.* **2015,** *15* (9), 6386-6396.

1119

1120   (58)   Chen, B.B.; Shi, C.; Crocker, M.; Wang, Y.; Zhu, A.M. Catalytic removal of formaldehyde at
1121   room temperature over supported gold catalysts. *Appl. Catal., B* **2013,** *132*, 245-255.

1122

1123   (59)   Zhang, C.; Li, Y.; Wang, Y.; He, H. Sodium-Promoted Pd/TiO$_2$ for Catalytic Oxidation of
1124   Formaldehyde at Ambient Temperature. *Environ. Sci. Technol.* **2014,** *48* (10), 5816-5822.

1125   (60)   Xu, Z.; Yu, J.; Jaroniec, M. Efficient catalytic removal of formaldehyde at room temperature
1126   using AlOOH nanoflakes with deposited Pt. *Appl. Catal., B* **2015,** *163*, 306-312.

1128   (61)   Li, D.; Yang, G.; Li, P.; Wang, J.; Zhang, P. Promotion of Formaldehyde Oxidation over Ag
1129   Catalyst by Fe Doped MnO_x Support at Room Temperature. *Catal. Today* **2016,** *277*, 257-265.

1131   (62)   Zhang, Y.; Shen, Y.; Yang, X.; Sheng, S.; Wang, T.; Adebajo, M. F.; Zhu, H. Gold catalysts
1132   supported on the mesoporous nanoparticles composited of zirconia and silicate for oxidation of
1133   formaldehyde. *J. Mol. Catal. A: Chem.* **2010,** *316*, 100-105.

1135   (63)   Li, C., Shen, Y.; Jia, M.; Sheng, S.; Adebajo, M. O.; Zhu, H. Catalytic combustion of
1136   formaldehyde on gold/iron-oxide catalysts. *Catal. Commun.* **2008,** *9* (3), 355-361.

1138   (64)   Xu, Q.; Lei, W.; Li, X.; Qi, X.; Yu, J.; Liu, G.; Wang, J.; Zhang, P. Efficient Removal of
1139   Formaldehyde by Nanosized Gold on Well-Defined CeO_2 Nanorods at Room Temperature.
1140   *Environ. Sci. Technol.* **2014,** *48* (16), 9702-9708.

1142   (65)   Chen, H.; Tang, M.; Rui, Z.; Ji, H. MnO_2 Promoted TiO_2 Nanotube Array Supported Pt Catalyst
1143   for Formaldehyde Oxidation with Enhanced Efficiency. *Ind. Eng. Chem. Res.* **2015,** *54* (36),
1144   8900-8907.

1146   (66)   Chen, Y.; He, J.; Tian, H.; Wang, D.;Yang, Q. Enhanced formaldehyde oxidation on Pt/MnO 2
1147   catalysts modified with alkali metal salts. *J. Colloid Interface Sci.* **2014,** *428*, 1-7.

1149   (67)   Fan, Z.; Zhang, Z.; Fang, W.; Yao, X.; Zou, G.; Shangguan, W. Low-temperature catalytic
1150   oxidation of formaldehyde over Co_3O_4 catalysts prepared using various precipitants. *Chin. J.*
1151   *Catal.* **2016,** *37* (6), 947-954.

1153   (68)   Wang, Y.; Zhu, A.; Chen, B.; Crocker, M.; Shi, C. Three-dimensional ordered mesoporous Co–
1154   Mn oxide: A highly active catalyst for "storage–oxidation" cycling for the removal of
1155   formaldehyde. *Catal. Commun.* **2013,** *36*, 52.

1157   (69)   Xia, Y.; Dai, H.; Zhang, L.; Deng, J.; He, H.; Au, C.T. Ultrasound-assisted nanocasting
1158   fabrication and excellent catalytic performance of three-dimensionally ordered mesoporous
1159   chromia for the combustion of formaldehyde, acetone and methanol. *Appl. Catal., B* **2010,** *100*
1160   (1), 229-237.

1162   (70)   Bai, B.; Arandiyan, H.; Li, J. Comparison of the performance for oxidation of formaldehyde on
1163   nano-Co_3O_4, 2D-Co_3O_4, and 3D-Co_3O_4 catalysts. *Appl. Catal., B* **2013,** *142*, 677-683.

1165   (71)   Dai, Z.; Yu, X.; Huang, C.; Li, M.; Su, J.; Guo, Y.; Xu, H.; Ke, Q. Nanocrystalline MnO_2 on an
1166   activated carbon fiber for catalytic formaldehyde removal. *RSC Adv.* **2016,** *6* (99), 97022-97029.

1168   (72)   Feng, Q.; Kanoh, H.; Ooi, K. Manganese oxide porous crystals. *J. Mater. Chem.* **1999,** *9* (2), 319-
1169   333.

1171   (73)   Wang, J.; Zhang, P.; Li, J.; Jiang, C.; Yunus, R.; Kim, J. Room-Temperature Oxidation of
1172   Formaldehyde by Layered Manganese Oxide: Effect of Water. *Environ. Sci. Technol.* **2015,** *49*
1173   (20), 12372-12379.

(74) Wang, J.; Li, J.; Jiang, C.; Zhou, P.; Zhang, P.; Yu, J. The effect of manganese vacancy in birnessite-type MnO_2 on room-temperature oxidation of formaldehyde in air. *Appl. Catal., B* **2017,** *204*, 147-155.

(75) Wang, J.; Zhang, G.; Zhang, P. Layered birnessite-type MnO_2 with surface pits for enhanced catalytic formaldehyde oxidation activity. *J. Mater. Chem. A* **2017,** *5* (12), 5719.

(76) Bai, B.; Qiao, Q.; Li, J.; Hao, J. Synthesis of three dimensional ordered mesoporous MnO2 and its catalytic performance in formaldehyde oxidation. *Chin. J. Catal.* **2016,** *37*, 27-31.

(77) Zhou, L.; Zhang, J.; He, J.; Hu, Y.; Tian, H. Control over the morphology and structure of manganese oxide by tuning reaction conditions and catalytic performance for formaldehyde oxidation. *Mater. Res. Bull.* **2011,** *46* (10), 1714-1722.

(78) Wu, Y.; Ma, M.; Zhang, B.; Gao, Y.; Lu, W.; Guo, Y. Controlled synthesis of porous Co3O4 nanofibers by spiral electrospinning and their application for formaldehyde oxidation. *RSC Adv.* **2016,** *6*, 102127-102133.

(79) Zeng, L.; Li, K.; Huang, F.; Zhu, X.; Li, H. Effects of Co_3O_4 nanocatalyst morphology on CO oxidation: Synthesis process map and catalytic activity. *Chin. J. Catal.* **2016,** *37*, 908-922.

(80) Huang, Y.; Long, B.; Tang, M.; Rui, Z.; Balogun, M.S.; Tong, Y.; Ji, H. Bifunctional catalytic material: An ultrastable and high-performance surface defect CeO 2 nanosheets for formaldehyde thermal oxidation and photocatalytic oxidation. *Appl. Catal., B* **2016,** *181*, 779-787.

(81) Zeng, L.; Song, W.; Li, M.; Zeng, D.; Xie, C. Catalytic oxidation of formaldehyde on surface of H TiO2/H C TiO2 without light illumination at room temperature. *Appl. Catal., B* **2014,** *147*, 490-498.

(82) Zhou, L.; He, J.; Zhang, J.; He, Z.; Hu, Y.; Zhang, C.; He, H. Facile In-Situ Synthesis of Manganese Dioxide Nanosheets on Cellulose Fibers and their Application in Oxidative Decomposition of Formaldehyde. *J. Phys. Chem. C* **2011,** *15* (34), 16873-16878.

(83) Imamura, S.; Shono, M.; Okamoto, N.; Hamada, A.; Ishida, S. Effect of cerium on the mobility of oxygen on manganese oxides. *Appl. Catal., A* **1996,** *142* (2), 279-288.

(84) Luo, M. F.; Ma, J. M.; Lu, J. Q.; Song, Y. P.; Wang, Y.J. High-surface area $CuO–CeO_2$ catalysts prepared by a surfactant-templated method for low-temperature CO oxidation. *J. Catal.* **2007,** *246* (1), 52-59.

(85) Ding, Z.Y.; Li, L.; Wade, D.; Gloyna, E.F. Supercritical water oxidation of NH_3 over a MnO_2/CeO_2 catalyst *Ind. Eng. Chem. Res.* **1998,** *37* (5), 1707-1716.

(86) Tang, X.; Li, Y.; Huang, X.; Xu, Y.; Zhu, H.; Wang, J.; Shen, W. $MnO_x–CeO_2$ mixed oxide catalysts for complete oxidation of formaldehyde: effect of preparation method and calcination temperature. *Appl. Catal., B* **2006,** *62* (3), 265-273.

(87) Lu, L.; Tian, H.; He, J.; Yang, Q. Graphene–MnO_2 Hybrid Nanostructure as a New Catalyst for Formaldehyde Oxidation. *J. Phys. Chem. C* **2016,** *120* (41), 23660-23668.

1224 (88) Lou, Y.; Cao, X.-M.; Lan, J.; Wang, L.; Dai, Q.; Guo, Y.; Ma, J.; Zhao, Z.; Guo, Y.; Hu, P.; Lu,
1225 G. Ultralow-temperature CO oxidation on an In_2O_3–Co_3O_4 catalyst: a strategy to tune CO
1226 adsorption strength and oxygen activation simultaneously. *Chem. Commun. (Cambridge, U.K.)*
1227 **2014,** *50* (52), 6835-6838.

1229 (89) Wang, Z.; Pei, J.; Zhang, J. Catalytic oxidization of indoor formaldehyde at room temperature–
1230 Effect of operation conditions. *Build. Environ.* **2013,** *65*, 49-57.

1232 (90) Wen, Y.; Tang, X.; Li, J.; Hao, J.; Wei, L.; Tang, X. Impact of synthesis method on catalytic
1233 performance of MnO_x–SnO_2 for controlling formaldehyde emission. *Catal. Commun.* **2009,** *10*
1234 (8), 1157-1160.

1236 (91) Bai, L.; Wyrwalski, F.; Lamonier, J.F.; Khodakov, A.Y.; Monflier, E.; Ponchel, A. Effects of β-
1237 cyclodextrin introduction to zirconia supported-cobalt oxide catalysts: From molecule-ion
1238 associations to complete oxidation of formaldehyde. *Appl. Catal., B* **2013,** *138*, 381-390.

1240 (92) Xuesong, L.; Jiqing, L.; Kun, Q.; Huang, W; Mengfei, L. A comparative study of formaldehyde
1241 and carbon monoxide complete oxidation on MnO_x-CeO_2 catalysts. *J. Rare Earths* **2009,** *27* (3),
1242 418-424.

1244 (93) Li, J.W.; Pan, K.L.; Yu, S.J.; Yan, S.Y.; Chang, M.B. Removal of formaldehyde over $MnxCe1−$
1245 xO_2 catalysts: Thermal catalytic oxidation versus ozone catalytic oxidation *J. Environ. Sci.* **2014,**
1246 *26*, 2546-2553.

1248 (94) Zhu, L.; Wang, J.; Rong, S.; Wang, H.; Zhang, P. Cerium modified birnessite-type MnO_2 for
1249 gaseous formaldehyde oxidation at low temperature. *Appl. Catal., B* **2017,** *211*, 212-221.

1251 (95) Shi, C.; Wang, Y.; Zhu, A.; Chen, B.; Au, C. $MnxCo_3−xO_4$ solid solution as high-efficient
1252 catalysts for low-temperature oxidation of formaldehyde. *Catal. Commun.* **2012,** *28*, 18-22.

1254 (96) Lu, S.; Li, K.; Huang, F.; Chen, C.; Sun, B. Efficient MnO_x-Co_3O_4-CeO_2 catalysts for
1255 formaldehyde elimination. *Appl. Surf. Sci.* **2017,** *400*, 277-282.

1257 (97) Sidheswaran, M. A.; Destaillats, H.; Sullivan, D. P.; Larsen, J.; Fisk, W. J. Quantitative room-
1258 temperature mineralization of airborne formaldehyde using manganese oxide catalysts. *Appl.*
1259 *Catal., B* **2011,** *107* (1), 34-41.

1261 (98) Li, J., Zhang, P., Wang, J. and Wang, M. Birnessite-Type Manganese Oxide on Granular
1262 Activated Carbon for Formaldehyde Removal at Room Temperature. *J. Phys. Chem. C* **2016,** *120*
1263 (42), 24121-24129.

1265 (99) Bai, B.; Li, J; Hao, J. 1D-MnO_2, 2D-MnO_2 and 3D-MnO_2 for low-temperature oxidation of
1266 ethanol. *Appl. Catal., B* **2015,** *164*, 241-250.

1268 (100) Sun, Y.; Zhang, W.; Li, D.; Gao, L.; Hou, C.; Zhang, Y.; Liu, Y. Facile synthesis of
1269 MnO_2/rGO/Ni composite foam with excellent pseudocapacitive behavior for supercapacitors. *J.*
1270 *Alloys Compd.* **2015,** *649*, 579-584.

1272 (101) Zhang, C.; He, H.; Tanaka, K.I. Catalytic performance and mechanism of a Pt/TiO_2 catalyst for
1273 the oxidation of formaldehyde at room temperature. *Appl. Catal., B* **2006,** *65* (1), 37-43.

1275   (102)   Chen, B.B.; Zhu, X. B.; Crocker, M.; Wang, Y.; Shi, C. FeO x-supported gold catalysts for
1276   catalytic removal of formaldehyde at room temperature. *Appl. Catal., B* **2014,** *154*, 73-81.
1277

1278   (103)   Yu, J.; Li, X.; Xu, Z.; Xiao, W. NaOH-Modified Ceramic Honeycomb with Enhanced
1279   Formaldehyde Adsorption and Removal Performance. *Environ. Sci. Technol.* **2013,** *47* (17),
1280   9928-9933.

List of Tables

Table 1. Noble metal supported catalysts for formaldehyde oxidation

Table 2. Single transition metal catalysts for HCHO oxidation

Table 3. Transition metal composite catalysts for HCHO oxidation

Table 4. Immobilized transition metal catalysts for HCHO oxidation

Table 1

Catalyst	Preparation method	Reaction conditions	HCHO conversion/removal	Reference
1 wt% Pd/TiO$_2$	Deposition precipitation-reduction	500 mg catalyst, 10 ppm HCHO, air, 50% [3]RH, 120,000 mL/g·h [5]GHSV	[2]100% at 25°C	(33)
1 wt% Au/CeO$_2$	Deposition precipitation (using urea)	250 mg catalysts,80 ppm HCHO, 21%O$_2$/N$_2$, 50% [3]RH, 34,000/h [5]GHSV	[1]100% at 25°C	(58)
1 wt% Au/CeO$_2$	Deposition precipitation (using NaOH)	250 mg catalyst, 80 ppm HCHO, 21%O$_2$/N$_2$, 50% [3]RH, 34,000/h [5]GHSV	[1]100% at 70°C	(58)
2 wt% Na−1 wt% Pd/TiO$_2$	Impregnation-reduction	65 mg catalyst, 140 ppm HCHO, 20% O$_2$, 25% [3]RH, 95,000/h [5]GHSV	[1]100% at 25°C	(59)
0.8 wt% Pt/AlOOH	Impregnation-reduction	100 mg catalyst, 138 ppm HCHO, air, 25% [3]RH	[2]96.82% [4](25°C,1h)	(60)
0.8 wt% Pt/TiO$_2$	Impregnation-reduction	100 mg catalyst, 138 ppm HCHO, air, 25% [3]RH	[2]96.82% [4](25°C,1h)	(60)
Ag/CeO$_2$ (nanosphere)	Hydrothermal synthesis	50 mg catalyst, 810 ppm HCHO, 20% O$_2$, and balance N$_2$, 84,000/h [5]GHSV	[1]100% at 110°C	(47)
Ag/3D-Co$_3$O$_4$	Deposition-precipitation	200 mg catalyst, 100 ppm HCHO, 20% O$_2$, 30,000/h [5]GHSV	[1]100% at 100°C	(46)
1.7wt% K- Ag/3D-Co$_3$O$_4$	Deposition-precipitation	200 mg catalyst, 100 ppm HCHO, 20% O$_2$, 30,000/h [5]GHSV	[1]100% at 70°C [1]55% at 27°C	(46)
8.9 wt% Ag/3D- MnO$_2$	Deposition-precipitation	200 mg catalyst, 500 ppm HCHO, 20% O$_2$, 60,000/h [5]GHSV	[1]100% at 110°C	(43)
Ag/MnO$_2$	Redox-reaction	200 mg catalyst, 230 ppm HCHO, air, static reactor	[1]76% [4](25°C,1h)	(61)
Ag/Fe$_{0.1}$- MnO$_2$	Redox-reaction	200 mg catalyst, 230 ppm HCHO, air, static reactor	[1]100% [4](25°C, 1h)	(61)
Ag/MnO$_2$	Redox-reaction	200 mg catalyst, 400 ppm HCHO, 21% O$_2$, 30,000 mL/g·h [5]GHSV, dynamic system	[1]100% at 120°C	(61)
Ag/Fe$_{0.1}$- MnO$_2$	Redox-reaction	200 mg catalyst, 400 ppm HCHO, 21% O$_2$, 30,000 mL/g·h [5]GHSV, dynamic system	[1]100% at 90°C	(61)
3DOM-Au/CeO$_2$	Nanocasting: Polystyrene colloidal crystal hard templates	200 mg catalyst, 0.06% HCHO, purified air, 66,000 mL/ g·h [5]GHSV	[1]100% at 75°C	(44)
0.85 wt% Au/ZrO$_2$-silicate	Deposition	200 mg catalyst, 90 mg/m^3 HCHO, purified air, 52,000 ml/g·h [5]GHSV	[1]100% at 157°C	(62)
3 wt% Au/CeO$_2$	Deposition-precipitation	50 mg catalyst, 500 ppm HCHO, 20% O$_2$, 35,400/h [5]GHSV	[1]92.3% at 37°C and [1]100% at 50°C	(37)
7.10 wt% Au/Fe$_2$O$_3$	Co-precipitation	200 mg catalyst, 6.25mg/m^3 HCHO, compressed air, 54,000 ml/g·h [5]GHSV	[1]100% at 80°C	(63)
1.8 wt % Au/CeO$_2$	Deposition-precipitation	150 mg catalyst, 109.3 ppm HCHO, air, static reactor	[2]90% (25°C, 1h)	(64)
2 wt Pt/urchin-like MnO$_2$	RT redox reaction	100 mg catalyst, 460 ppm, purified air 20,000 mL/ g·h [5]GHSV	[1]100% at 80°C	(41)

2 wt% Pt/cocoon-like MnO2	Redox reaction under acidic condition	100 mg catalyst, 460 ppm HCHO, purified air 20,000 mL/g·h [5]GHSV	[1]100% at 90°C	(*41*)
Pt/OMS-2	Redox reaction plus impregnation	200 mg catalyst, 500 ppm HCHO, 10% O_2, 30,000 ml/ g·h [5]GHSV	[1]100% at 120°C	(*45*)
0.2 wt% Pt/0.5 wt% MnO_2/TiO_2 (Nanotubes)	Electrochemical anodization plus impregnation	200 mg catalyst, 50 ppm HCHO, 20% O_2, 35% [3]RH, 30,000 ml/g·h [5]GHSV	[2]95% at 30°C	(*65*)
0.1 wt% Pt/TiO_2	Impregnation-reduction	500 mg catalyst, 10 ppm HCHO, air, 50% [3]RH, 80,000/h [5]GHSV	[2]99.1% at 25°C	(*24*)
2 wt% Na-1 wt% Pt/MnO_2 (birnessite)	Deposition-precipitation	100 mg catalyst, 200 ppm HCHO, purified air, 30,000 mL/g·h [5]GHSV	[1]100% at 50°C	(*66*)
NaOH modified - 1 wt% Pt/TiO_2	Impregnation-reduction	300 mg catalyst, 253 ppm HCHO, air, static reactor	[2]94.07% [4](25°C, 1h)	(*27*)
1 wt% Pt/TiO_2	Impregnation	100 ppm HCHO, 20 vol% O_2, 50,000/h [5]GHSV	[1]100% at 20°C	(*22*)
1 wt% Rh/TiO_2	Impregnation	100 ppm HCHO, 20 vol% O_2, 50,000/h [5]GHSV	[1]100% at 80°C	(*22*)
1 wt% Pd/TiO_2	Impregnation	100 ppm HCHO, 20 vol% O_2, 50,000/h [5]GHSV	[1]100% at 120°C	(*22*)
3D 3wt% Au/ CeO_2-Co_3O_4 (2.5:1, Ce/Co)	Nanocasting: 3D-PS hard template	200 mg catalyst, 8 ppm HCHO, purified air, 15,000 mL/g·h [5]GHSV	[1]100% at 36°C	(*50*)
2D 1wt% Au/ Co_3O_4-CeO_2 (7:3 Co:Ce)	Nonocasting: SBA-15 hard template	100 mg catalyst, 200 ppm HCHO, 22% O_2, 55,000/h [5]GHSV	[1]50% at 25°C	(*51*)
3 wt% Pt/MnO_x-CeO_2 (M.R = 0.5)	Impregnation	200mg catalyst, 30-580 ppm HCHO, 20% O_2, 30,000 mL/g·h [5]GHSV	[1]100% at 25°C	(*48*)

[1] Conversion = $[CO_2]_{out}$ / $[HCHO]_{in}$

[2] Removal = $([HCHO]_{in} - [HCHO]_{out})$ / $[HCHO]_{in}$

[3] RH - Relative humidity

[4] Indicates the reaction temperature and time taken to reach stated removal/conversion in a static reactor.

[5]GHSV- Gas hourly space velocity (h^{-1} or ml/g.h)

Table 2

Catalyst	Preparation method	Reaction conditions	HCHO conversion/removal	Reference
Birnessite	Hydrothermal synthesis using surfactant (SDS)	100 mg catalyst, 460 ppm HCHO, purified air, 30,000 ml/g·h [5]GHSV	[1]100% at 100°C	(54)
Birnessite	Redox Reaction of KMnO$_4$ and Ammonium oxalate	100 mg catalyst , 40 ppm HCHO, air, 80% [3]RH, 120,000 ml/g·h,	[1]90% at 96°C	(74)
Birnessite	Surface modification of birnesite with nitric acid and Tetraammonium hydroxide	100 mg catalyst, 200 ppm HCHO, air, , 45% [3]RH, 120,000 ml/g·h [5]GHSV	[1]100% at 100°C	(75)
Todorokite	Na-Birnesite followed by MgCl$_2$ hydrothermal treatment	200 mg catalyst, 400 ppm HCHO, 10.0% O$_2$, 18,000 ml/g·h [5]GHSV	[1]100% at 160°C	(55)
Pyrolusite	Redox hydrothermal synthesis	200 mg catalyst, 400 ppm HCHO, 10.0% O$_2$, 18,000 ml/g·h [5]GHSV	[1]100% at 180°C	(55)
K-OMS-2 nanoparticle	Soft chemistry (KMnO$_4$ and benzyl alcohol) using surfactant (CTAB) at 25°C	100 mg catalyst, 460 ppm HCHO, purified air, 20,000 ml/g·h [5]GHSV	[1]64% at 100°C.	(56)
K-OMS-2 nanorod	Soft chemistry (KMnO$_4$ and benzyl alcohol) using surfactant (CTAB) at 100°C	100 mg catalyst, 460 ppm HCHO, purified air, 20,000 ml/g·h [5]GHSV	[1]10% at 100°C	(56)
K-OMS-2 nanorods	Sol-gel synthesis at 70°C	100 mg catalyst, 460 ppm HCHO, 21% O$_2$, 30,000 ml/g·h [5]GHSV	[1]100% at 200°C	(36)
K-OMS-2 nanoparticles	Sol-gel synthesis at 15°C	100 mg catalyst, 460 ppm HCHO, 21% O$_2$, 30,000 ml/g·h [5]GHSV	[1]54% at 200°C	(36)
OMS-2	Redox reaction	200 mg catalyst, 500 ppm HCHO, 10% O$_2$, 30,000 ml/g·h [5]GHSV	[1]100% at 120°C	(45)
3D-MnO$_2$ mesoporous	Nanocasting: KIT-6 hard template	200 mg catalyst, 400 ppm HCHO, 20% O$_2$, 30,000 ml/g·h [5]GHSV	[1]100% at 130°C	(76)
α-MnO$_2$ nanorods	Redox-hydrothermal synthesis	200 mg catalyst, 400 ppm HCHO, 20% O$_2$, 30,000 ml/g·h [5]GHSV	[1]100% at 140°C	(76)
β-MnO$_2$ nanorods	Redox-hydrothermal synthesis	200 mg catalyst, 400 ppm HCHO, 20% O$_2$, 30,000 ml/g·h [5]GHSV	[1]100% at 180°C	(76)
8.86% MnO$_2$/cellulose (nanosheet birnessite)	KMnO$_4$ impregnation followed by oleic acid reduction	60 mg catalyst, 100 ppm HCHO, 20% O$_2$, 50, 000/h [5]GHSV	[2]100% at 140°C	(82)
Birnessite nanospheres	KMnO$_4$-oleic acid hydrothermal reduction	50 mg catalyst, 100 ppm HCHO, 20% O$_2$, 50,000/h [5]GHSV	[2]100% at 140°C	(77)
Cryptomelane nanorods	KMnO$_4$-oleic acid hydrothermal reduction	50 mg catalyst, 100 ppm HCHO, 20% O$_2$, 50,000/h [5]GHSV	[2]95.1% at 140°C	(77)
Ramsdellite nanorods	KMnO$_4$ oleic acid hydrothermal reduction	50 mg catalyst, 100 ppm HCHO, 20% O$_2$, 50,000/h [5]GHSV	[2]87.2% at 140°C	(77)
Monoclinic MnOOH	KMnO$_4$ oleic acid hydrothermal reduction	50 mg catalyst, 100 ppm HCHO, 20% O$_2$, 50,000/h [5]GHSV	[2]90.1% at 140°C	(77)

KxMnO$_2$ mesoporous hollow nanospheres	Low concentration KMnO$_4$-oleic acid reduction	50 mg catalyst, 100 ppm HCHO, 20% O$_2$, 50,000/h [5]GHSV	[2]100% at 80°C	(21)
KxMnO$_2$ mesoporous honeycomb nanospheres	High concentration KMnO$_4$-oleic acid reduction	70 mg catalyst, 100 ppm HCHO, 20% O$_2$, 50,000/h	[2]100% at 85°C	(21)
Birnessite	Facile redox-reaction	50 mg catalyst, 200 ppm HCHO, synthetic air, static reactor	[2]100% [4](25°C,12h)	(73)
α-MnO$_2$	Hydrothermal synthesis	60 mg catalyst, 170 ppm HCHO, 20% O$_2$, 25% [3]RH, 100,000 mL/g·h [5]GHSV	[1]100% at 125°C	(19)
β-MnO$_2$	Hydrothermal synthesis	60 mg catalyst, 170 ppm HCHO, 20% O$_2$, 25% [3]RH, 100,000 mL/g·h [5]GHSV	[1]100% at 200°C	(19)
γ-MnO$_2$	Hydrothermal synthesis	60 mg catalyst, 170 ppm HCHO, 20% O$_2$, 25% [3]RH, 100,000 mL/g·h [5]GHSV	[1]100% at 150°C	(19)
δ-MnO$_2$	Hydrothermal synthesis	60 mg catalyst, 170 ppm HCHO, 20% O$_2$, 25% [3]RH, 100,000 mL/g·h [5]GHSV	[1]100% at 80°C	(19)
Spinel Co$_3$O$_4$	Precipitation with KHCO$_3$	100 mg catalyst, 100 ppm HCHO, 21% O$_2$, 69,000/h [5]GHSV	[1]100% at 90°C	(67)
Spinel Co$_3$O$_4$	Precipitation with NH$_4$HCO$_3$ and 2% K$_2$CO$_3$ treatment	100 mg catalyst, 100 ppm HCHO, 21% O$_2$, 69,000/h [5]GHSV	[1]100% at 90°C	(67)
Spinel Co$_3$O$_4$	Precipitation with KOH	100 mg catalyst, 100 ppm HCHO, 21% O$_2$, 69,000/h	[1]100% at 120°C	(67)
Spinel Co$_3$O$_4$	Precipitation with NH$_3$·H$_2$O	100 mg catalyst, 100 ppm HCHO, 21% O$_2$, 69,000/h [5]GHSV	[1]100% at 130°C	(67)
3D- Co$_3$O$_4$	Nanocasting: KIT-6 hard template	200 mg catalyst, 400 ppm HCHO, 20% O$_2$, 30,000 ml/g·h [5]GHSV	[1]100% at 130°C	(70)
2D- Co$_3$O$_4$	Nanocasting: SBA-15 hard template	200 mg catalyst, 400 ppm HCHO, 20% O$_2$, 30,000 ml/g·h [5]GHSV	[1]100% at 150°C	(70)
Nano- Co$_3$O$_4$	Precipitation with Na$_2$CO$_3$	200 mg catalyst, 400 ppm HCHO, 20% O$_2$, 30,000 ml/g·h [5]GHSV	[1]100% at 230°C	(70)
3D- Co$_3$O$_4$	Nanocasting: KIT-6 hard template	200 mg catalyst, 100 ppm HCHO, 20% O$_2$, 30,000/h [5]GHSV	[1]100% at 110°C	(46)
3D-Cr$_2$O$_3$	Nanocasting: KIT-6 hard template	100 mg catalyst, 500 ppm HCHO, 30,000 ml/g·h [5]GHSV	[1]90% at 117°C	(69)
2D- Co$_3$O$_4$	Nanocasting: SBA-15 hard template	100 mg catalyst, 200 ppm HCHO, 22% O$_2$, 55,000/h [5]GHSV	[1]20.3% at 25°C	(51)
Co$_3$O$_4$ nanofibers	spiral electrospinning synthesis, calcined at 500°C	100 mg catalyst, 400 ppm HCHO, 20% O$_2$, 30,000 mL/g·h [5]GHSV	[1]100% at 98°C	(78)
4% Eu doped-CeO$_2$ nanosheets	Anodic electrodeposition of Eu onto CeO$_2$	200 mg catalyst, 50 ppm HCHO, 25% O$_2$, 30,000mL/g·h [5]GHSV	[2]100% at 120°C	(80)
H-TiO$_2$	Hydrothermal synthesis	100 mg catalyst, 100 ppm HCHO, air, static reactor	[2]53% at [4](25°C,4h)	(81)

[1] Conversion = [CO$_2$] out / [HCHO] in

[2] Removal = ([HCHO] in - [HCHO] out) / [HCHO] in

[3] RH - relative humidity

[4] Indicates the reaction temperature and time taken to reach such conversion in a static reactor.

Table 3

Catalyst	Preparation method	Reaction conditions	HCHO conversion/removal	Reference
MnO_x-CeO_2	Co-precipitation	200 mg catalyst, 580 ppm HCHO, 18% O_2, 21,000 mL/g·h [4]GHSV	[1]100% at 100°C	(86)
MnO_x-CeO_2	Co-precipitation	200 mg catalyst, 580 ppm HCHO, 20% O_2, 30,000 mL/g·h [4]GHSV	[1]90% at 90°C	(48)
$Mn_{0.5}Ce_{0.5}O_2$	Co-precipitation	300 mg catalyst, 33 ppm HCHO, 21% O_2, 10,000/h [4]GHSV	[2]100% at 270°C	(93)
$Mn_{0.5}Ce_{0.5}O_2$	Co-precipitation	300 mg catalyst, 61 ppm HCHO, 21% O_2/506 ppm HCHO O_3, 10,000/h [4]GHSV	[2]100% at 25°C	(93)
MnO_x-CeO_2	Co-precipitation	200mg catalyst, 580 ppm HCHO, 20% O_2, 30,000 mL/g·h [4]GHSV	[1]100% at 125°C	(92)
Ce-MnO_2	Redox reaction of $KMnO_4$ and Ammonium oxalate with Cerium nitrate	100 mg catalyst, 190 ppm HCHO, air, 90 L/g·h [4]GHSV	[1]100% at 100°C	(94)
3D-CeO_2- Co_3O_4	Nanocasting: 3D-PS hard template	200 mg catalyst, 8 ppm HCHO, purified air, 15,000 mL/g·h [4]GHSV	[1]100% at 155°C	(50)
Co-Mn	Co-precipitation	150 mg catalysts, 80 ppm HCHO, 21% O_2, 50% [3]RH, 60,000/h [4]GHSV	[1]100% at 75°C	(95)
3D-Co-Mn	Nanocasting: KIT 6 Hard template	250 mg catalyst, 80 ppm HCHO, 21% O_2, 50% [3]RH, 36,000/h [4]GHSV	[1]100% at 70°C	(68)
MnO_x-Co_3O_4-CeO_2	Sol-gel synthesis	50 mg catalyst, 200 ppm HCHO, 21% O_2, 36,000 ml/g·h [4]GHSV	[1]100% at 100°C	(96)
MnO_x-SnO_2	Redox co-precipitation	200 mg catalyst, 400 ppm HCHO, 10% O_2, 30,000 ml/g·h [4]GHSV	[1]100% at 180°C	(90)
MnO_x-SnO_2	co-precipitation	200 mg catalyst, 400 ppm HCHO, 10% O_2, 30,000 ml/g·h [4]GHSV	[1]100% at 220°C	(90)
Graphene−MnO_2 hybrid	Graphene treatment with $KMnO_4$ (redox)	100 mg catalyst, 100 ppm HCHO, purified air, 30,000 mL/g·h [4]GHSV	[1]100% at 65°C	(87)

[1] Conversion = $[CO_2]_{out}$ / $[HCHO]_{in}$
[2] Removal = $([HCHO]_{in} - [HCHO]_{out})$ / $[HCHO]_{in}$
[3] RH - relative humidity
[4]GHSV- Gas hourly space velocity (h^{-1} or ml/g.h)

Table 4

Catalyst	Preparation method	Reaction conditions	HCHO removal	Reference
δ-MnO_2/PET 2	Redox-precipitation	500 mg catalyst, 0.6 mg/m^3 HCHO, purified air, 50% RH, 17,000/h [2]GHSV	94% at 25°C	(18)
8.86 wt% MnO_2/cellulose fiber 2	$KMnO_4$ impregnation of cellulose fiber followed by oleic acid treatment	5 mg catalyst, 100 ppm HCHO HCHO, 20 vol % O_2, 50 000/h [2]GHSV	99.1% at 140°C	(82)
Birnessite/AC 2	$KMnO_4$ reduction of	200 mg catalyst, 400 ppm HCHO, synthetic air	100% [1](25°C,7h)	(98)
δ-MnO_2/AC 2	Redox co-precipitation	100 mg catalyst, 150 ppm HCHO, pure air	100% [1](25°C,9h)	(71)

[1] Indicates the reaction temperature and time taken to reach such conversion in a static reactor.
[2]GHSV- Gas hourly space velocity (h^{-1} or ml/g.h)

7

Figure Captions

Figure 1. (a) Effect of birnessite calcination temperature on HCHO oxidation activity at room temperature. (b) HCHO conversion and CO_2 generation (*73*). "Reproduced with permission from Wang, J.; Zhang, P.; Li, J.; Jiang, C.; Yunus, R.; Kim, J. Room-Temperature Oxidation of Formaldehyde by Layered Manganese Oxide: Effect of Water. Environ. Sci. Technol. 2015, 49 (20), 12372-12379. Copyright (2015) American Chemical Society".

Figure 2. Effect of HCHO concentration on Pt/MnO_x-CeO_2 activity at room temperature. Reprinted (*48*). (Reproduced with permission from Tang, X.; Chen, J.; Huang, X.; Xu, Y.; Shen, W. Pt/MnO_x–CeO_2 catalysts for the complete oxidation of formaldehyde at ambient temperature. Appl. Catal., B 2008, 81 (1), 115-121. Copyright, 2008 Elsevier).

Figure 3. Concentration variation of HCHO and CO_2 formation in a static experiment: (a) over birnessite-MnO_2/AC (*98*) "Reproduced with permission from Li, J., Zhang, P., Wang, J. and Wang, M. Birnessite-Type Manganese Oxide on Granular Activated Carbon for Formaldehyde Removal at Room Temperature. J. Phys. Chem. C 2016, 120 (42), 24121-24129. Copyright (2016) American Chemical Society" and (b) over δ-MnO_2/AC (*71*). (Reproduced from Dai, Z.; Yu, X.; Huang, C.; Li, M.; Su, J.; Guo, Y.; Xu, H.; Ke, Q. Nanocrystalline MnO_2 on an activated carbon fiber for catalytic formaldehyde removal. RSC Adv. 2016, 6 (99), 97022-97029, with permission from The Royal Society of Chemistry).

Figure 4. Effect of reaction condition on the evolution of morphology and structure manganese based catalysts (*77*). (Reproduced with permission from Zhou, L.; Zhang, J.; He, J.; Hu, Y.; Tian, H. Control over the morphology and structure of manganese oxide by tuning reaction conditions

and catalytic performance for formaldehyde oxidation. Mater. Res. Bull. 2011, 46 (10), 1714-1722. Copyright, 2011 Elsevier).

Figure 5. Effect of tunnel structure on the complete oxidation of HCHO (*55*). (Reproduced with permission from Chen, T.; Dou, H.; Li, X.; Tang, X.; Li, J.; Hao, J. Tunnel structure effect of manganese oxides in complete oxidation of formaldehyde. Microporous Mesoporous Mater. 2009, 122 (1), 270-274. Copyright, 2009 Elsevier).

Figure 6. Formaldehyde conversion over transition metal catalysts as a function of reaction temperature.

Figure 7. Formaldehyde conversion over transition metal catalysts as a function of reaction time in a static system.

Figure 8. Synergistic Oxygen transfer mechanism in MnO_x-CeO_2 composites (*48*). (Reproduced with permission from Tang, X.; Chen, J.; Huang, X.; Xu, Y.; Shen, W. Pt/MnO_x–CeO_2 catalysts for the complete oxidation of formaldehyde at ambient temperature. Appl. Catal., B 2008, 81 (1), 115-121. Copyright, 2008 Elsevier).

Figure 9. Mechanism of HCHO oxidation on birnessite at RT (*73*). "Reproduced with permission from Wang, J.; Zhang, P.; Li, J.; Jiang, C.; Yunus, R.; Kim, J. Room-Temperature Oxidation of Formaldehyde by Layered Manganese Oxide: Effect of Water. Environ. Sci. Technol. 2015, 49 (20), 12372-12379. Copyright (2015) American Chemical Society".

Figure 10. Mechanism of HCHO oxidation over mesoporous Co_3O_4, Au/Co_3O_4, and Au/Co_3O_4-CeO_2 catalysts at RT (*51*). "Reproduced with permission from Ma, C.; Wang, D.; Xue, W.; Dou, B.; Wang, H.; Hao, Z. Investigation of Formaldehyde Oxidation over Co_3O_4−CeO_2 and Au/Co_3O_4−CeO_2 Catalysts at Room Temperature: Effective Removal and Determination of

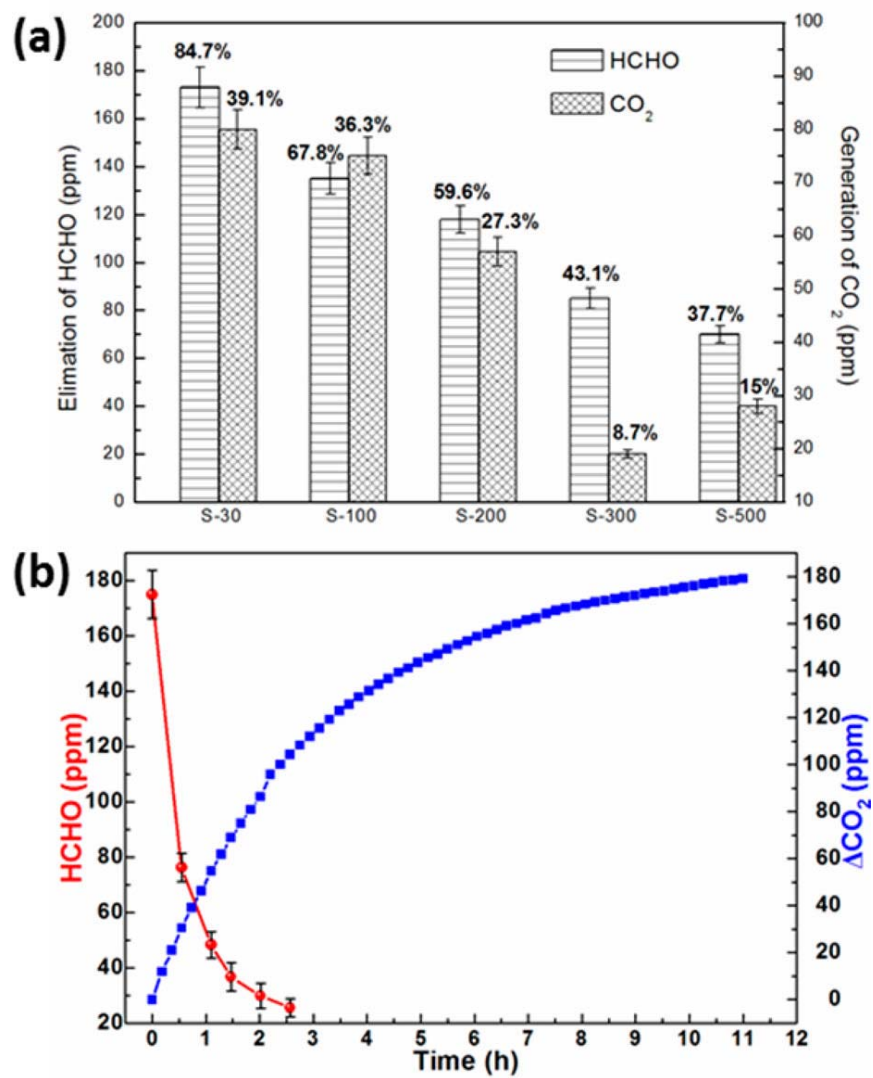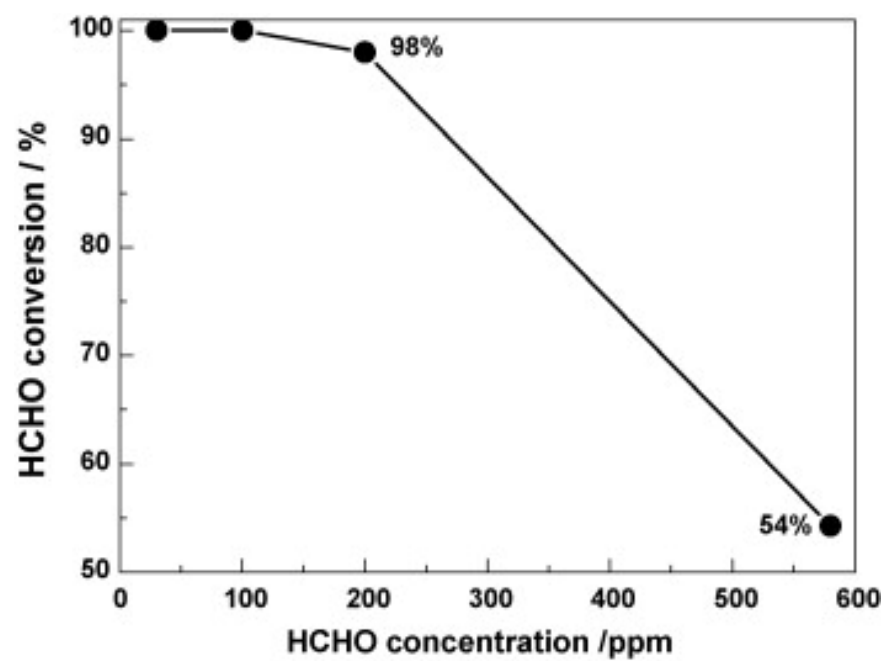Reaction Mechanism. Environ. Sci. Technol. 2011, 45 (8), 3628-3634. Copyright (2011) American Chemical Society".
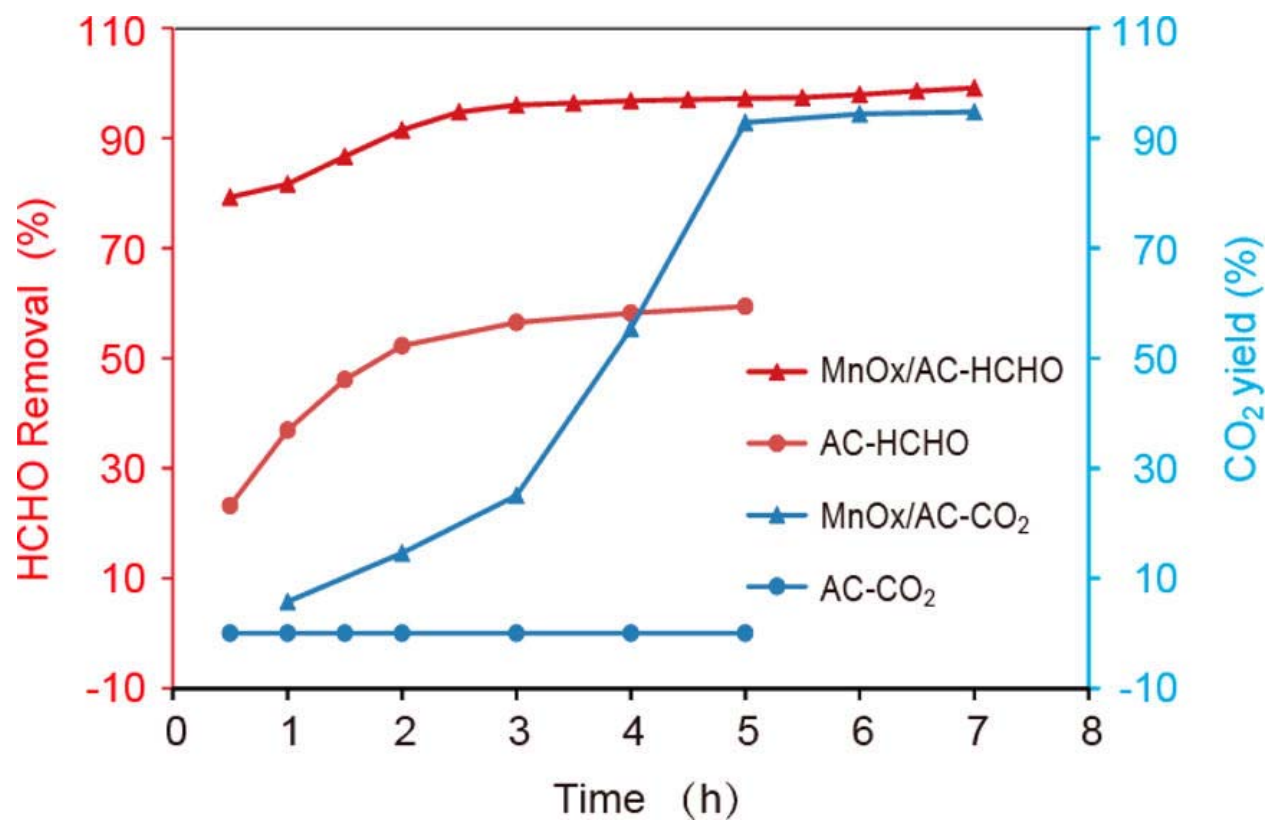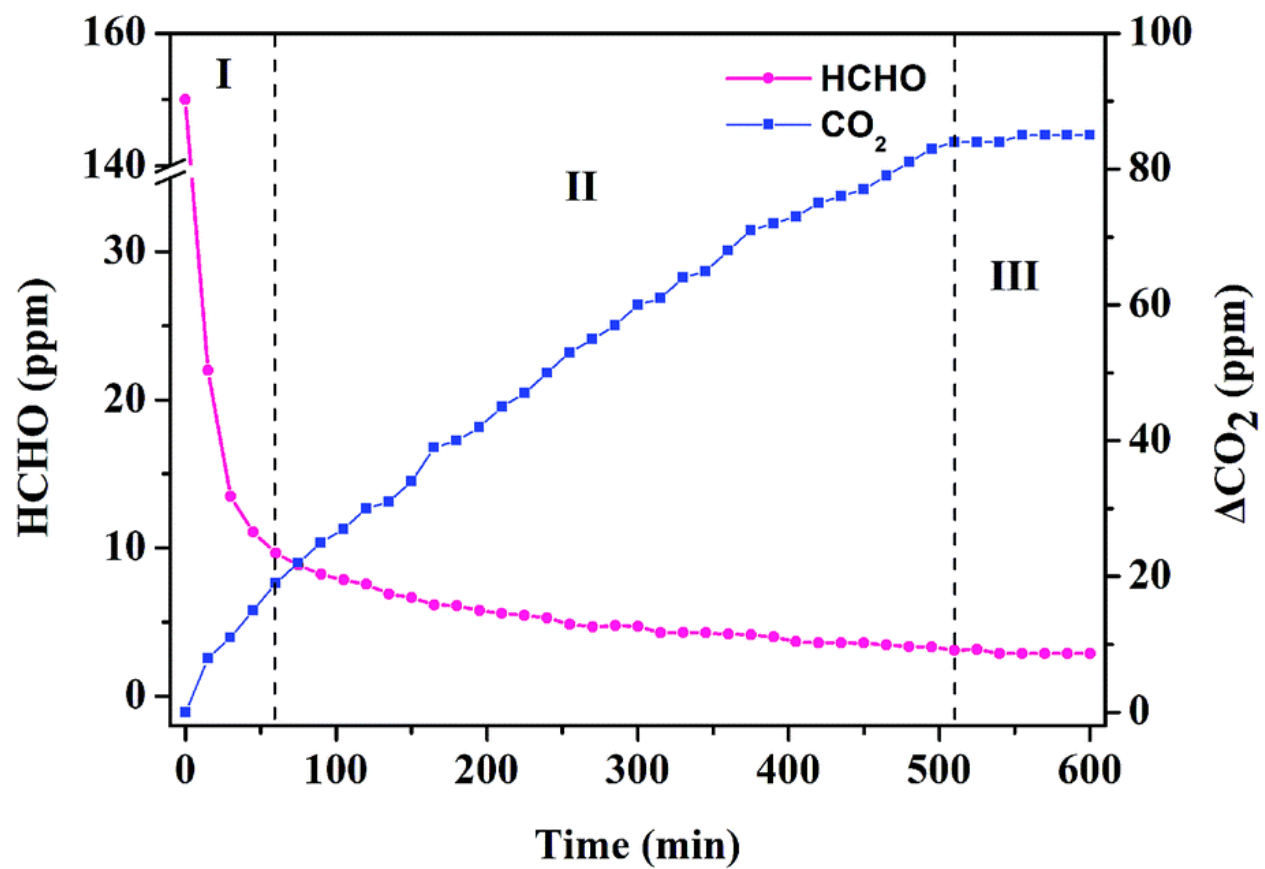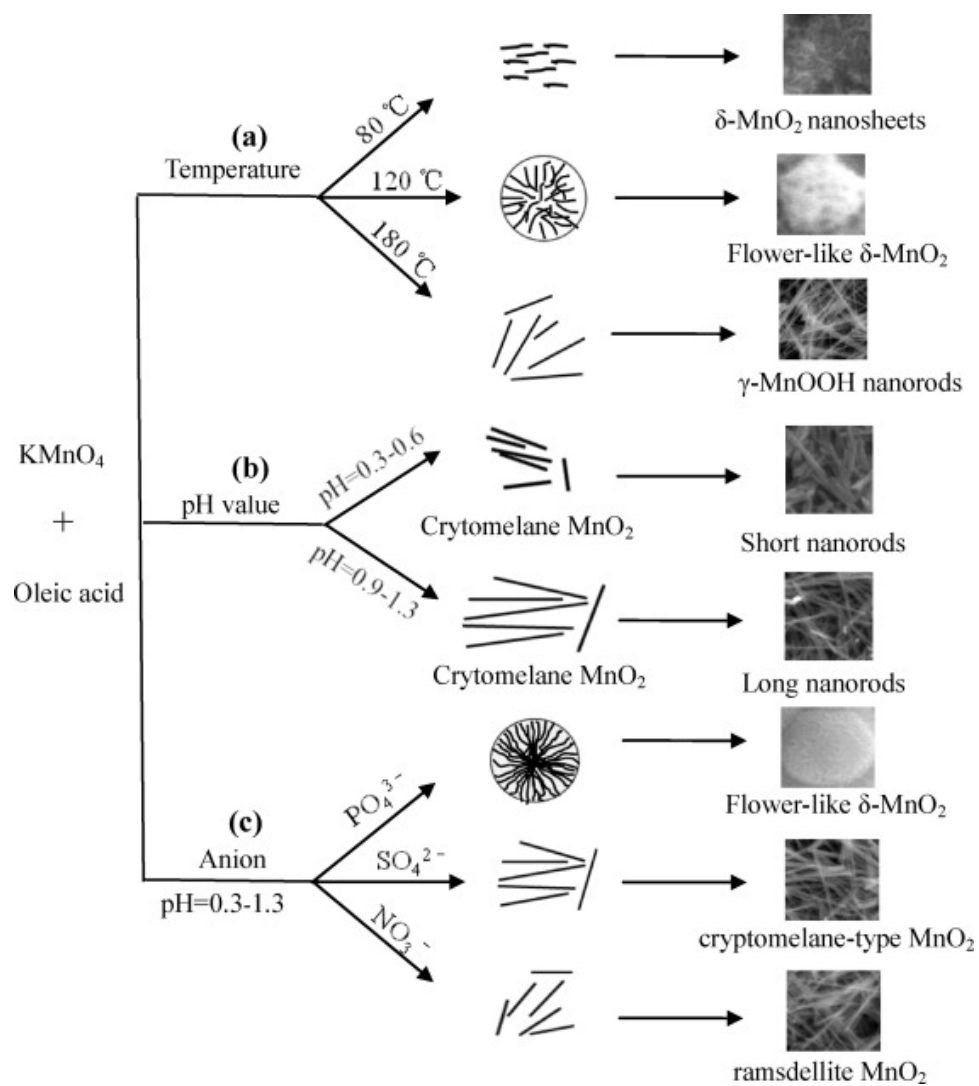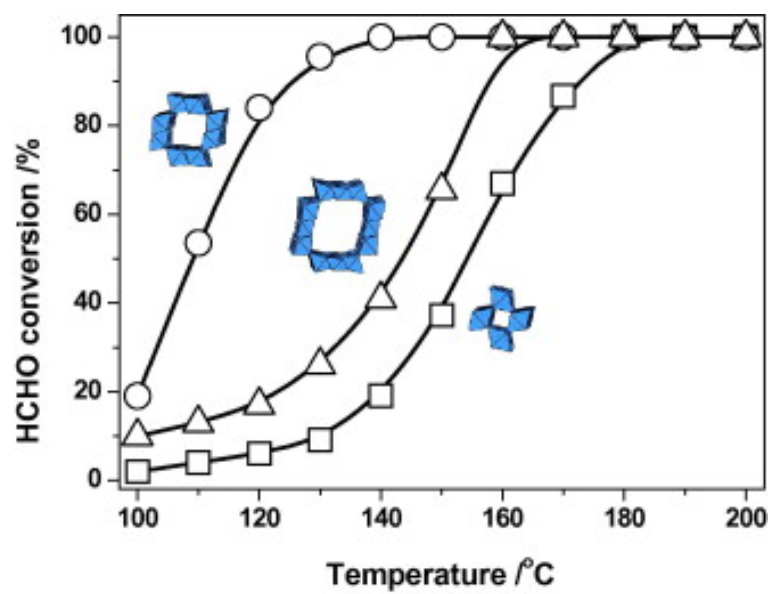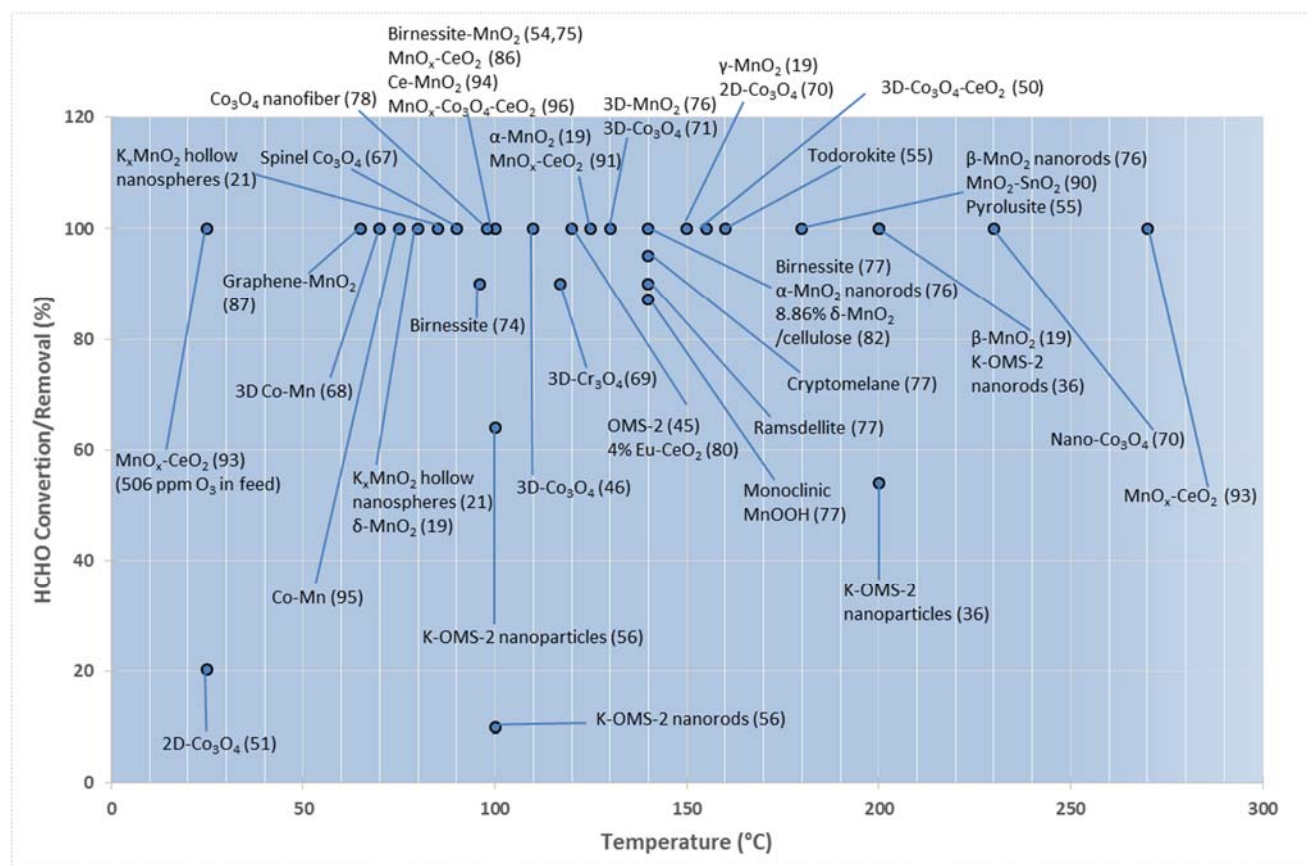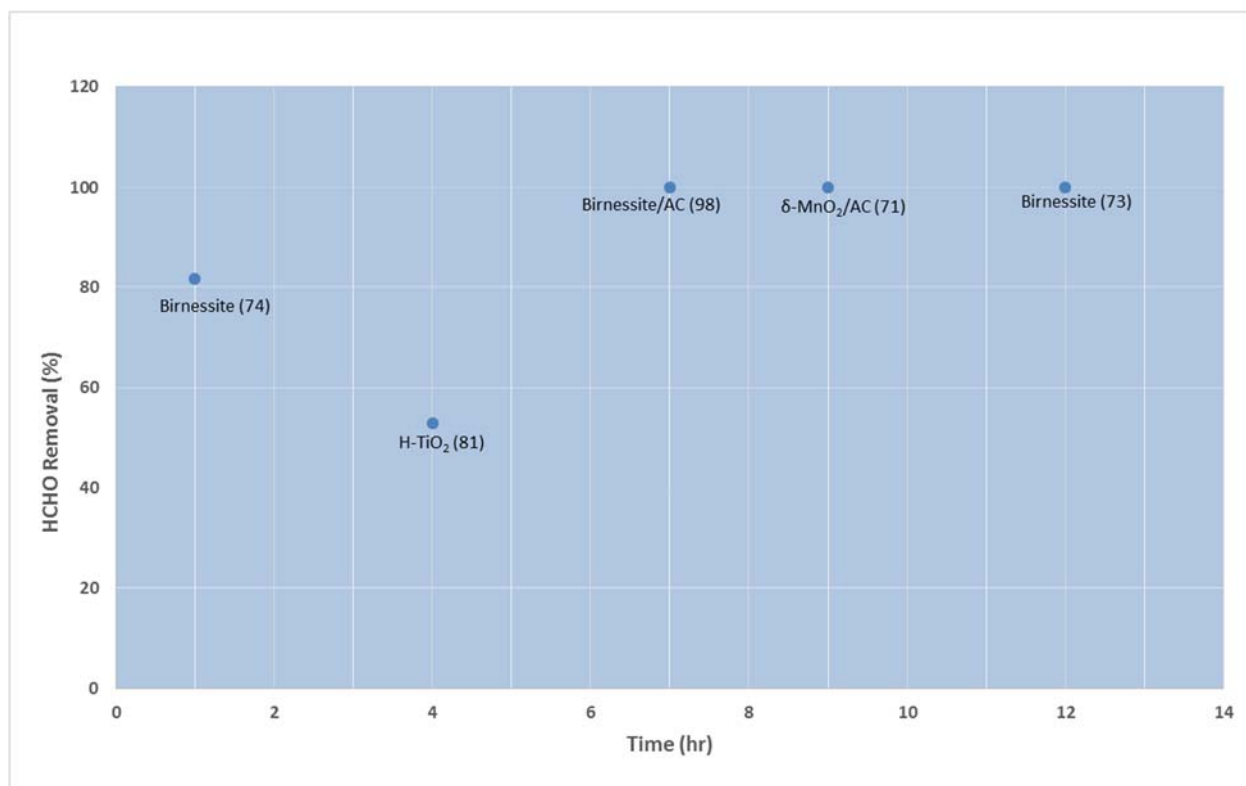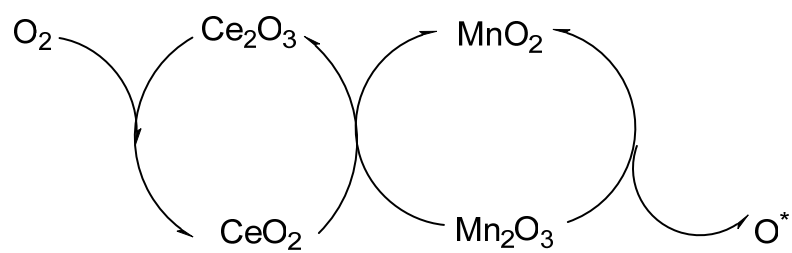
Figure 1

Figure 2

Figure 3(a)

Figure 3(b)

Figure 4

Figure 5

Figure 6

Figure 7

Figure 8

Figure 9

Figure 10